The link between accretion mode and environment in radio-loud active galaxies

J. Ineson,[1] J. H. Croston,[1,2] M. J. Hardcastle,[3] R. P. Kraft,[4] D. A. Evans,[4] and M. Jarvis[5,3,6]

[1]*School of Physics and Astronomy, University of Southampton, Southampton SO17 1BJ, UK*
[2]*Institute of Continuing Education, University of Cambridge, Madingley Hall, Madingley, CB23 8AQ, UK.*
[3]*School of Physics, Astronomy and Mathematics, University of Hertfordshire, Hatfield, Hertfordshire AL10 9AB, UK*
[4]*Harvard-Smithsonian Center for Astrophysics, 60 Garden Street, Cambridge, MA 02138, USA*
[5]*Astrophysics, Department of Physics, Keble Road, Oxford OX1 3RH, UK*
[6]*Department of Physics, University of the Western Cape, Private Bag X17, Bellville 7535, South Africa*

ABSTRACT

The interactions between radio-loud AGN and their environments play an important rôle in galaxy and cluster evolution. Recent work has demonstrated fundamental differences between High and Low Excitation Radio Galaxies (HERGs and LERGs), and shown that they may have different relationships with their environments. In the Chandra Large Project ERA (Environments of Radio-loud AGN), we made the first systematic X-ray environmental study of the cluster environments of radio galaxies at a single epoch ($z \sim 0.5$), and found tentative evidence for a correlation between radio luminosity and cluster X-ray luminosity. We also found that this relationship appeared to be driven by the LERG sub-population (Ineson et al. 2013).

We have now repeated the analysis with a low redshift sample ($z \sim 0.1$), and found strong correlations between radio luminosity and environment richness and between radio luminosity and central density for the LERGs but not for the HERGs. These results are consistent with models in which the HERGs are fuelled from accretion discs maintained from local reservoirs of gas, while LERGs are fuelled more directly by gas ingested from the intra-cluster medium.

Comparing the samples, we found that although the maximum environment richness of the HERG environments is similar in both samples, there are poorer HERG environments in the $z \sim 0.1$ sample than in the $z \sim 0.5$ sample. We have therefore tentative evidence of evolution of the HERG environments. We found no differences between the LERG sub-samples for the two epochs, as would be expected if radio and cluster luminosity are related.

Key words: galaxies: active, galaxies: clusters: intracluster medium, galaxies: jets

1 INTRODUCTION

The feedback cycles of radio-loud AGN play an important rôle in galaxy evolution (e.g. Croton et al. 2006; Sijacki & Springel 2006; Martizzi et al. 2014; Schaye et al. 2015), and we need to understand the processes that affect their behaviour in order to model galaxy formation and development. Over the past few years, compelling evidence has been uncovered for the importance of the dichotomy in the spectral types of radio-loud AGN — the High and Low Excitation Radio Galaxies (HERGs, also known as radio-loud radiative mode AGN, and LERGs, or jet-mode AGN) — and their different processes, environments and rôles in galaxy evolution. The current state of play is covered comprehensively in the reviews by McNamara & Nulsen (2012) and Heckman & Best (2014), so we will restrict ourselves to a brief description of the observational evidence and processes of interest for this paper.

The two types of radio galaxy have different accretion rates (e.g. Best & Heckman 2012; Son et al. 2012; Mingo et al. 2014; Gürkan et al. 2014; Fernandes et al. 2015), with the majority of HERGs having Eddington ratios of $\gtrsim$ 1 per cent and LERGs of $\lesssim$ 1 per cent, albeit with some overlap. The host galaxies display a different evolutionary phase, with HERGs tending to have lower mass than LERGs (e.g. Tasse et al. 2008; Smolčić 2009; Best & Heckman 2012), to be bluer (e.g. Smolčić 2009; Janssen et al. 2012; Herbert et al. 2010), and to have ongoing star formation (eg. Hardcastle et al. 2013).

The dichotomy in accretion rate appears to be related to different accretion methods. HERGs, in common with radio-quiet radiative mode AGN, are thought to be fuelled by cold gas which builds some form of accretion disc and gives rise to radiatively efficient accretion (Shakura & Sunyaev 1973). The radiation from the accretion disc indirectly gives rise to X-ray emission from the nucleus

and IR from the surrounding dusty torus. Cold fuel is channelled into the galaxy centre, and because the host galaxies have a plentiful supply of cold gas, there is also fuel available for star formation. The high accretion rate adds mass to the black hole, and radiative mode AGN are thought to be responsible for black hole growth and the bulge-black hole mass relation (e.g. Ishibashi & Fabian 2012).

Galaxy mergers and interactions are thought to be a major source of new gas for HERGs. The predicted galaxy merger rates of Hopkins et al. (2008) reproduced the observed population properties of QSOs – luminosity functions, fractions and clustering – suggesting that mergers and interactions could be a triggering and fueling mechanism. Ramos Almeida et al. (2012) looked for signs of interactions in HERGs and comparable quiescent galaxies and found a substantially higher proportion of HERGs than quiescent galaxies with comparably bright interaction features (90 per cent vs 50 per cent), implying that interactions are likely to be part of the triggering process. (Since interaction features endure for substantially longer than the active phase of a HERG, they calculated that we should expect HERGs in 1-10 per cent of disturbed ellipticals.) Tadhunter et al. (2014) estimated that gas reservoirs of around $10^9 M_\odot$ are required to sustain activity over the expected duty cycle of a HERG. They found that this matched observed HERG gas reservoirs whereas the reservoirs for quiescent galaxies are, on average, lower. The fact that there are also quiescent galaxies with large gas reservoirs suggests that the size of the reservoir alone is not sufficient to trigger activity, and that gas distribution and kinematics also play a part.

The fuelling mechanism for LERGs is more uncertain. They do not show the characteristic optical and X-ray features of radiatively efficient accretion seen in radiative mode AGN, and it is likely that they are fuelled by a hot, radiatively inefficient flow or advection dominated accretion flow (ADAF, e.g. Narayan & Yi 1994). Bondi accretion of hot gas could provide enough energy for the lower luminosity population (Allen et al. 2006; Hardcastle et al. 2007b), so such sources could be fuelled by a form of hot flow, but this is probably insufficient for the more luminous sources (Russell et al. 2013, – although this is disputed by Fujita et al. 2014). A number of researchers (e.g. Pizzolato & Soker 2005; Gaspari et al. 2012, 2013; Voit & Donahue 2015) discuss a process of chaotic accretion of cool gas clouds, which they find to be capable of releasing more than sufficient energy for the most powerful sources. In this model, filaments and blobs of cooling gas are channelled in from the ICM at large radii to form a central, rotating torus, and these gas clumps then collide and accrete, with both processes releasing energy. The cycle is controlled by the central entropy, which reduces the gas movement into the centre when high, but then drops again as the cold gas in the centre is accreted and removed by the jets. This allows the gas inflow to increase. Temperatures, accretion rates and jet powers thus vary (and in the case of lower power systems may turn off) during a well-regulated cycle that can be maintained for perhaps 10^8 years.

Looking now at the cluster environments of the radio-loud AGN, the radio jets transport energy a considerable distance into the cluster, and are themselves affected by the intra-cluster medium. A common feature of all proposed LERG fuelling models is that they obtain material from within the ICM, so do the properties of the large-scale cluster environment in their turn affect the feedback loop maintaining the AGN, or are the AGN properties solely determined by the more local environment of the host galaxy? And how does does this disruption of the cluster environment affect its evolution?

It has been suggested for some time that there is a differ-

ence between the environments of HERGs and LERGs. At lower redshifts ($z \lesssim 0.4$), the consensus of a number of studies is that HERGs appear to occupy a narrow range of relatively sparse environments compared with LERGs (e.g. Best 2004; Hardcastle 2004; Gendre et al. 2013). There is also some evidence that HERGs occupied richer environments in earlier epochs (e.g. Harvanek et al. 2001; Belsole et al. 2007; Ramos Almeida et al. 2013), suggesting evolution of the large-scale environment; conversely, Wold et al. (2000) and McLure & Dunlop (2001) found no evidence of evolution.

There are also mixed results when looking for relationships between radio luminosity and the cluster environment. Best (2004) found a correlation for LERGs but not for HERGs in the lower redshift range, as did Ineson et al. (2013) at $z \sim 0.5$. Belsole et al. (2007) found no correlation for a mixed sample of mainly HERGs at higher redshifts, while Wold et al. (2000), again at higher redshifts, found a correlation for QSOs.

There are a number of different measures of cluster richness, so comparing results needs some caution. Belsole et al. (2007) and Ineson et al. (2013) used X-ray luminosity within the virial radius and R_{500} respectively. The other studies cited above all used optical methods – a variation on the 'nearest neighbours' method (Best 2004); galaxy counts above a specified magnitude within 1 Mpc radius (Gendre et al. 2013); and the galaxy-galaxy spatial covariance function B_{gg} calculated within a variety of radii depending on the image size (Harvanek et al. 2001; Hardcastle 2004; Wold et al. 2000 use 0.5 Mpc; McLure & Dunlop 2001 use 180 kpc; Ramos Almeida et al. 2013 use 170 kpc). The different measures of cluster richness correlate, (e.g. Wold et al. 2000; Yee & Ellingson 2003; Ledlow et al. 2003; Ineson et al. 2013), but with a large amount of scatter so conversion between the methods is unreliable.

The different sizes of galaxy count regions may also present a problem. Tasse et al. (2008) calculated galaxy overdensities within three different radii (75 kpc, 250 kpc and 450 kpc). Differences between 250 and 450 kpc were present but not strong, but the results for 75 kpc, which would capture interacting galaxies, were strikingly different from the larger-scale radii. The HERG-dominated population in particular was very overdense within 75 kpc but underdense within the higher radii. Studies using galaxy count regions with large and small radii may therefore be capturing different effects.

Furthermore, if there is evolution of the environment, studies of environment richness at high and low redshift may not be directly comparable and studies covering a wide redshift range are at risk of confounding factors. In addition, the Malmquist bias in flux-limited samples, the changes in HERG and LERG populations with redshift and the paucity of powerful local sources also need to be taken into account during sample selection and data analysis. The studies cited above all agree on the differences between HERG and LERG environments at relatively low redshifts; the disagreements come when making comparisons across wider redshift ranges.

In the ERA (Environments of Radio-loud AGN) programme, we are making a systematic examination of the effects of epoch and environment on the properties of radio-loud AGN in order to address the two questions separately: is radio luminosity is related to the large-scale cluster environment? and does the environment evolve with epoch? In phase 1 (Ineson et al. 2013, I13 hereafter), we used the ERA sample (Figure 1) to compare radio luminosity and the hot gas environment within a limited redshift range ($0.4 < z < 0.6$), thus removing the effects of redshift evolution. We found that the LERGs occupied a wide range of environments,

and that there was a correlation between radio luminosity and environment richness. In contrast, the HERGs occupied a smaller range of environment richnesses and showed no sign of a correlation. Herbert et al. (2015), using the galaxy-quasar covariance function rather than the X-ray luminosity of the ICM found a similar result in the same redshift range, as did Best (2004) with a lower redshift sample ($z < 0.1$).

In this paper, we continue the ERA programme by making a similar analysis of a low redshift comparison sample with $z \sim 0.1$, to see if the results from the ERA sample carry across to the lower redshift, and if there is any evidence of environment change with epoch.

Throughout this paper we use a cosmology in which $H_0 = 70$ km s^{-1} Mpc^{-1}, $\Omega_{\mathrm{m}} = 0.3$ and $\Omega_\Lambda = 0.7$. Unless otherwise stated, errors are quoted at the 1σ level.

2 THE SAMPLE

The new sample, hereafter referred to as the z0.1 sample, consists of all radio-loud AGN with visible structure beyond the nucleus lying in the redshift range $0.01 \leqslant z \leqslant 0.2$ from two flux-limited radio surveys: the 3CRR survey (Laing et al. 1983) and the subsample of the 2Jy survey (Wall & Peacock 1985; Tadhunter et al. 1993) defined by Dicken et al. (2008). The initial sample contained 38 3CRR and 22 2Jy sources, but five sources were excluded. 3C 382 has currently no suitable *Chandra* or *XMM-Newton* observation, 3C 83.1B, 3C 264 and Abell 1552 lie in the outskirts of richer clusters, so that their immediate environments could not be disentangled from those of the stronger sources for the spherical modelling, while the angular size of the cluster emission of 3C 84 (Perseus A) is so large that analysis was impractical. The final sample consists of 55 sources comprising 25 HERGs and 30 LERGS. 22 of the sources have FRI morphologies, and 33 are FRIIs.

The properties of the sources are listed in Table 1 and Figure 1 shows radio luminosity plotted against redshift. The ERA sample sources used in I13 are also shown in Figure 1. Positions, radio luminosities, spectral type and morphologies of the sources were taken from the on-line 3CRR catalogue[1] and from Mingo et al. (2014). Redshifts were taken from the most recent source cited in the 3CRR catalogue, Mingo et al. (2014), the NASA/IPAC Extragalactic Database (NED)[2] and the SIMBAD astronomical database[3]. Galactic column densities came from Dickey & Lockman (1990) via the HEASARC tools.

3 OBSERVATIONS AND DATA PREPARATION

3.1 X-ray data

All but two of the X-ray observations for the z0.1 sample came from the *Chandra* archive; for 3C 31 and 3C 66B we used observations from the *XMM-Newton* archive. The *XMM-Newton* observations used the three EPIC cameras with the medium filter and the *Chandra* observations used either the ACIS-S3 chip or the four ACIS-I chips. Observation IDs and times are given in Table 2.

Initial data processing for the *Chandra* observations was done in the same way as in I13, using the *Chandra* analysis package

CIAO v4.5 and CALDB v4.5.8. The files were reprocessed using *chandra_repro*, with particle background cleaning for observations in the VFAINT mode, and background flares were removed using *deflare*. Screened observation times are included in Table 2.

Since the clusters and groups at $z \sim 0.1$ had a larger angular size than the more distant observations in I13, in some cases extending beyond the observing chip, two additional processes were used. In order to correct for vignetting, aspect, chip edges and gaps, we created exposure maps using the *fluximage* script. We also built background files from the *Chandra* blank sky datasets for each observation using the method described in the CIAO threads[4]. These were used when generating surface brightness profiles and spectra.

The *XMM-Newton* events files were processed in the same way as in I13, using using *XMM-Newton* SAS v11.0.0. The reprocessed events files were checked for flares and then corrected for vignetting using *evigweight*. Again, the particle background in the *XMM-Newton* sources was removed using the method described by Croston et al. (2008a) using the closed filter files supplied courtesy of E. Pointecouteau.

Both the *Chandra* blank sky files and the *XMM-Newton* closed filter files were scaled by comparing the source and background count rates at 10-12 keV (ACIS and MOS cameras) and 12-14 keV (pn camera). The background file count rates were scaled by this factor. Note that the *Chandra* blank sky files are cleaned, open filter datasets and so can be used to model the ACIS background as well as to remove instrumental background whereas the *XMM-Newton* closed filter files remove only the instrumental background.

We checked for pileup by finding the maximum count rate per pixel at the peak of the emission, which we scaled to estimate the pileup fraction[5]. If pileup was greater than 12 per cent, we checked the maximum count rate per pixel at increasing radii until pileup was less than 12 per cent. We then excluded the central region out to this radius. One source had severe pileup (3C 390.3), and three had mild pileup (3C 219, 3C 303 and NGC 6251).

For both the *Chandra* and *XMM-Newton* sources, we examined images of the sources in *ds9*, overlaying them with the radio contours. We identified point sources in the data sets and emission associated with the radio lobes, which we excluded during subsequent analysis.

3.2 Radio data

Radio maps were used to mask out the radio lobes so that any radio-related X-ray emission did not contaminate our measurements of the cluster properties. All of the 3CRR radio maps except that of NGC 7385 were taken from the 3CRR Atlas[6]. We also used existing maps for the majority of the 2Jy sources. The remaining six maps were made using observations from the VLA and ATCA archives and reduced using AIPS in the standard manner.

Table 2 contains the full details of the radio maps used, including references.

4 ANALYSIS

The aim of the analysis was to find the temperature and X-ray luminosity of the ICM emission of the radio galaxies. Where possible,

---

Table 1. The z0.1 sample

Source	RA (J2000) Dec		Redshift	Scale	$\log_{10} L_{151}$	Type	FR	nH
	h m s	deg min sec		kpc arcsec^{-1}	W Hz^{-1} sr^{-1}		Morphology	x10^{20} cm^{-2}
3C 28	00 55 50.65	+26 24 37.3	0.195	3.23	26.24	LERG	2	5.39
3C 31	01 07 24.96	+32 24 45.2	0.017	0.34	24.30	LERG	1	5.36
3C 33	01 08 52.86	+13 20 14.2	0.060	1.15	25.93	HERG	2	3.90
3C 35	01 12 02.26	+49 28 35.5	0.067	1.28	25.34	LERG	2	13.00
3C 66B	02 23 11.41	+42 59 31.5	0.021	0.43	24.68	LERG	1	9.15
3C 76.1	03 03 14.99	+16 26 19.0	0.033	0.65	24.73	LERG	1	10.60
3C 98	03 58 54.43	+10 26 02.8	0.031	0.62	25.28	HERG	2	15.10
3C 192	08 05 35.01	+24 09 49.7	0.060	1.15	25.53	HERG	2	4.21
3C 219	09 21 08.63	+45 38 57.3	0.174	2.95	26.52	HERG	2	1.51
3C 236	10 06 01.76	+34 54 10.2	0.099	1.83	25.82	LERG	2	1.23
3C 285	13 21 17.86	+42 35 14.8	0.079	1.50	25.51	HERG	2	1.27
3C 293	13 52 17.80	+31 26 46.4	0.045	0.89	25.04	LERG	1	1.29
3C 296	14 16 52.98	+10 48 27.2	0.025	0.50	24.50	LERG	1	1.88
3C 303	14 43 02.76	+52 01 37.2	0.141	2.48	25.75	HERG	2	1.58
3C 305	14 49 21.64	+63 16 14.0	0.042	0.82	25.08	HERG	1	1.70
3C 310	15 04 57.11	+26 00 58.3	0.054	1.05	25.87	LERG	1	3.70
3C 321	15 31 43.46	+24 04 19.0	0.096	1.78	25.76	HERG	2	4.11
3C 326	15 52 09.10	+20 05 48.3	0.089	1.67	25.87	LERG	2	3.81
3C 338	16 28 38.29	+39 33 04.2	0.031	0.62	25.30	LERG	1	0.86
3C 346	16 43 48.60	+17 15 49.4	0.162	2.79	25.85	HERG	1	5.67
3C 386	18 38 26.22	+17 11 50.2	0.017	0.35	24.50	LERG	1	18.10
3C 388	18 44 02.35	+45 33 29.6	0.091	1.70	25.95	LERG	2	6.47
3C 390.3	18 42 08.93	+79 46 17.2	0.056	1.09	25.82	HERG	2	4.27
3C 433	21 23 44.56	+25 04 28.0	0.102	1.88	26.15	HERG	2	11.90
3C 442A	22 14 46.88	+13 50 27.2	0.026	0.53	24.70	LERG	1	5.07
3C 449	22 31 20.62	+39 21 30.1	0.017	0.35	24.16	LERG	1	12.00
3C 452	22 45 48.75	+39 41 15.9	0.081	1.53	26.21	HERG	2	11.30
3C 465	23 38 29.36	+27 01 53.4	0.030	0.61	25.15	LERG	1	5.01
4C 73.08	09 49 45.78	+73 14 23.1	0.059	1.14	25.34	HERG	2	2.29
DA 240	07 48 36.82	+55 48 59.5	0.036	0.71	25.07	LERG	2	4.52
NGC 6109	16 17 40.56	+35 00 15.7	0.030	0.59	24.61	LERG	1	1.33
NGC 6251	16 32 31.95	+82 32 16.4	0.025	0.50	24.39	LERG	1	5.65
NGC 7385	22 49 54.59	+11 36 32.5	0.026	0.53	24.43	LERG	1	5.11
PKS 0034-01	00 37 49.18	-01 09 08.2	0.073	1.40	25.54	LERG	2	3.07
PKS 0038+09	00 40 50.53	+10 03 26.8	0.188	3.14	26.44	HERG	2	5.51
PKS 0043-42	00 46 17.75	-42 07 51.4	0.116	2.10	26.23	LERG	2	2.21
PKS 0213-13	02 15 37.5	-12 59 30.5	0.147	2.57	26.23	HERG	2	1.92
PKS 0349-27	03 51 35.81	-27 44 33.8	0.066	1.26	25.55	HERG	2	0.99
PKS 0404+03	04 07 16.49	+03 42 25.8	0.089	1.66	25.89	HERG	2	11.90
PKS 0442-28	04 44 37.67	-28 09 54.6	0.147	2.57	26.33	HERG	2	2.43
PKS 0620-52	06 21 43.29	-52 41 33.3	0.051	1.00	25.12	LERG	1	5.17
PKS 0625-35	06 27 6.65	-35 29 16.3	0.055	1.06	25.41	LERG	1	7.24
PKS 0625-53	06 26 20.44	-53 41 35.2	0.054	1.05	25.35	LERG	2	5.42
PKS 0806-10	08 08 53.600	-10 27 39.71	0.109	1.99	25.92	HERG	2	7.74
PKS 0915-11	09 18 05.67	-12 05 44.0	0.055	1.07	26.21	LERG	1	4.93
PKS 0945+07	09 47 45.15	+07 25 20.4	0.086	1.62	25.91	HERG	2	3.00
PKS 1559+02	16 02 27.38	+01 57 55.7	0.104	1.91	26.12	HERG	2	6.44
PKS 1648+05	16 51 08.16	+04 59 33.8	0.155	2.69	27.14	LERG	1	6.33
PKS 1733-56	17 37 35.80	-56 34 03.4	0.099	1.82	26.13	HERG	2	8.29
PKS 1839-48	18 43 14.64	-48 36 23.3	0.111	2.02	25.83	LERG	1	5.62
PKS 1949+02	19 52 15.77	+02 30 23.1	0.059	1.14	25.53	HERG	2	14.30
PKS 1954-55	19 58 16.64	-55 09 39.7	0.058	1.13	25.57	LERG	1	4.52
PKS 2211-17	22 14 25.78	-17 01 36.3	0.153	2.66	26.37	LERG	2	2.61
PKS 2221-02	22 23 49.57	-02 08 12.4	0.056	1.09	25.48	HERG	2	4.87
PKS 2356-61	23 59 04.50	-60 54 59.1	0.096	1.78	26.27	HERG	2	2.38

the temperature was obtained by spectral analysis; when there were insufficient counts, it was estimated from the count rate in a self-consistent way, as described in Section 4.1. The luminosity was determined by integrating the surface brightness profiles to the R_{500} overdensity radius (defined in Section 4.1).

The appendix contains brief notes on the individual sources.

Table 2. Observation data for the z0.1 sample

Source Instrument	X-ray[a]	Observation ID	Exposure[b] time (ks)	Screened[b] time (ks)	Radio map freq. (GHz)	Resolution (arcsec)	Ref.
3C 28	C	3233	50.38	49.30	1.4	1.1×1.1	1
3C 31	XMM	551720101	50.00	24.00	0.61	52×29	1
3C 33	C	6910, 7200	39.83	39.61	1.5	4×4	1
3C 35	C	10240	25.63	25.63	1.4	14×12	1
3C 66B	XMM	0002970201	17.86	13.39	1.4	12×12	1
3C 76.1	C	9298	8.06	8.06	1.5	4.9×4.9	1
3C 98	C	10234	31.71	31.71	4.9	3.7×3.7	1
3C 192	C	9270	10.02	9.62	1.4	3.9×3.9	1
3C 219	C	827	19.24	16.79	1.5	1.4×1.4	1
3C 236	C	10249	40.50	40.50	0.61	28×28	1
3C 285	C	6911	39.62	39.61	1.5	5.5×5.5	1
3C 293	C	12712	67.81	67.22	1.5	7.6×7.6	1
3C 296	C	3968	49.43	48.91	1.5	4.9×4.9	1
3C 303	C	1623	15.10	14.95	1.5	1.2×1.2	1
3C 305	C	12797, 13211	57.32	57.31	1.5	0.15×0.15	1
3C 310	C	11845	57.58	57.16	1.5	4×4	1
3C 321	C	3138	47.13	46.87	1.5	1.4×1.4	1
3C 326	C	10908, 10242	45.81	45.81	1.4	14×39	1
3C 338	C	10748	40.58	40.58	4.9	1×1	1
3C 346	C	3129	46.69	39.91	1.5	0.35×0.35	1
3C 386	C	10232	29.29	29.29	1.5	5.8×5.8	1
3C 388	C	5295	30.71	30.31	1.4	1.3×1.3	1
3C 390.3	C	830	33.97	28.60	1.6	2.8×2.8	1
3C 433	C	7881	38.19	37.15	8.5	0.75×0.75	1
3C 442A	C	5635, 6353	40.99	40.79	1.4	7.5×7.5	1
3C 449	C	4057	29.18	24.99	0.61	30×48	1
3C 452	C	2195	79.92	79.53	1.4	6×6	1
3C 465	C	4816	49.53	49.49	1.4	5.4×5.4	1
4C 73.08	C	10239	28.52	28.52	0.61	30×30	1
DA 240	C	10237	24.08	24.08	0.61	34×34	1
NGC 6109	C	3985	19.39	13.42	1.4	13×13	1
NGC 6251	C	847	37.44	30.67	0.33	55×55	1
NGC 7385	C	10233	39.33	39.33	4.9	4.9×3.6	2
PKS 0034-01	C	2178	27.52	26.54	4.9	4.5×3.7	3
PKS 0038+09	C	9293	7.94	7.94	4.9	4.4×3.4	3
PKS 0043-42	C	10319	18.38	18.38	8.6	1.2×0.88	4
PKS 0213-13	C	10320	19.89	19.89	4.9	5.9×3.4	3
PKS 0349-27	C	11497	19.89	19.89	1.5	11×8.9	2
PKS 0404+03	C	9299	8.07	8.07	8.4	2.2×2.2	5
PKS 0442-28	C	11498	19.79	19.79	4.9	9.3×2.1	3
PKS 0620-52	C	11499	19.80	19.80	4.7	2.6×1.5	3
PKS 0625-35	C	11500	19.79	19.79	4.9	4.7×3.2	2
PKS 0625-53	C	4943	18.45	16.67	4.8	2×1.6	4
PKS 0806-10	C	11501	19.79	19.79	4.9	6.8×1.6	2
PKS 0915-11	C	4970	98.82	98.42	1.4	2×1.5	2
PKS 0945+07	C	6842	29.78	29.78	1.5	4×4	6
PKS 1559+02	C	6841	39.65	39.62	8.5	2.2×2.2	5
PKS 1648+05	C	6257	49.52	49.52	1.5	1.4×1.4	7
PKS 1733-56	C	11502	19.86	19.66	4.7	2.2×1.3	3
PKS 1839-48	C	10321	19.79	19.79	4.7	2.6×1.7	3
PKS 1949+02	C	2968	49.47	45.66	1.5	4.5×4.1	8
PKS 1954-55	C	11505	20.65	20.45	4.8	2.4×1.3	4
PKS 2211-17	C	15091	164.38	163.17	4.9	7.6×3.1	3
PKS 2221-02	C	7869	45.60	45.60	8.2	2.4×2.4	5
PKS 2356-61	C	11507	19.79	19.79	1.5	7.2×6.9	9

References: (1) http://www.jb.man.ac.uk/atlas, (2) Made from the VLA archives, (3) Morganti et al. (1993), (4) Morganti et al. (1999), (5) Leahy et al. (1997), (6) Hardcastle et al. (2007a), (7) Gizani & Leahy (2003), (8) Dennett-Thorpe et al. (2002), (9) Made from the ATCA archives. [a] C=*Chandra*, X=*XMM-Newton*. [b] pn camera times for *XMM-Newton* sources.
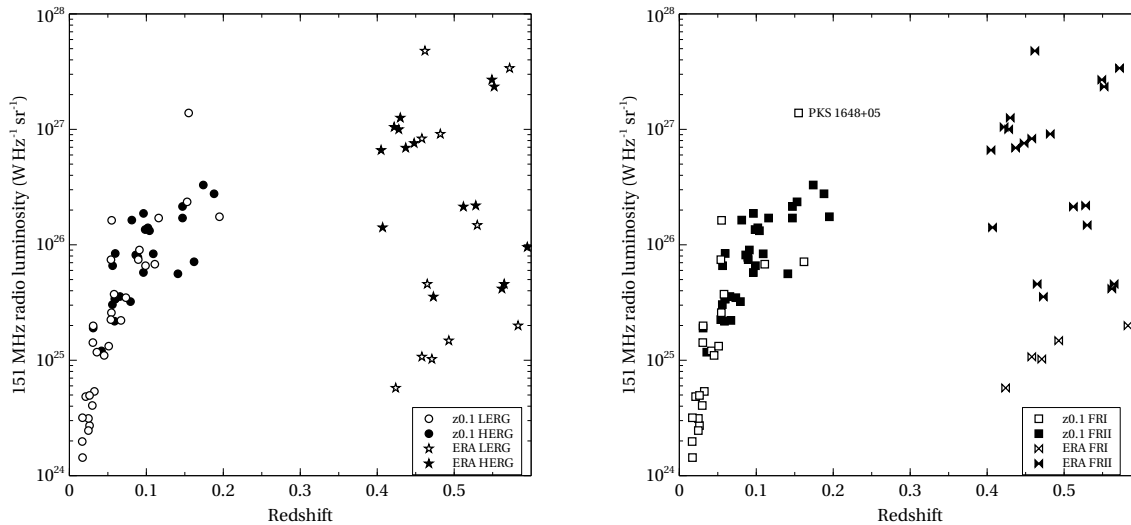
Figure 1. 151 MHz radio luminosity vs redshift for the z0.1 sample and the ERA ($z \sim 0.5$) sample used in I13. The left plot shows the HERG (filled symbols) and LERG (empty symbols) excitation classes and the right plot shows FRI (empty symbols) and FRII (filled symbols) morphologies. PKS 1648+05 has characteristics of both morphologies.

4.1 Spatial analysis

We extracted a radial surface brightness profile from the events file of each source by taking the average counts in annuli around the source centroid. The point sources and radio emission identified during data preparation were removed and the annulus areas adjusted to account for the excluded regions. We used an energy range of 0.4-7.0 keV, this being the well calibrated range for the *Chandra* data. When possible, we used a double subtraction method where the background in the blank sky/closed filter files was subtracted from the source file (see Markevitch et al. 2003) prior to generating the profile. Then, when the maximum detection radius lay at least partially within the ACIS-S3 or ACIS-I chips, we used an annulus outside the maximum detection radius to obtain the background counts remaining after the initial background subtraction, and these were subtracted from the source counts to obtain the net counts in each annulus.

For the *XMM-Newton* sources, since the pn camera is more sensitive than the MOS cameras, we created the pn profile first and then used the same annuli and background area for the MOS profiles. The three profiles were then scaled by their relative exposure times and added together.

Table 3 contains the maximum detection radius and net counts within that radius for each of the sources. If the emission extends beyond the chip, the maximum detection radius is quoted as the distance to the chip edge.

We fitted the surface brightness profiles with β models (Cavaliere & Fusco-Femiano 1976) in a similar manner to that described in I13, using the Markov-Chain Monte Carlo (MCMC) method described by Croston et al. (2008a) to explore the parameter space of these models and find Bayesian estimates of the core radii (r_c) and β values. However, since these sources are nearer than those in I13, their host galaxies usually extend beyond the instrument point spread function (PSF). In these cases, a second β model was added so that the inner and outer components were modelled individually.

We initially checked whether the PSF alone gave a satisfactory fit to the data, which was not the case for any of the sources. We then added a single β model to fit the extended emission, convolved

with the PSF. The unconvolved surface brightness at radius R is given by

$$S(R) = S_0(1 + (\frac{R}{r_c})^2)^{-3\beta+0.5} \tag{1}$$

where r_c is the core radius and S_0 is the normalisation.

If this gave a satisfactory fit, we checked whether the modelled emission extended beyond the host galaxy radius (taken from NED[7]). If it did not, which was the case for seven sources, we used the observations of the source to derive an upper limit on cluster-scale emission. For these sources, we compared the net count rate from a region outside the host galaxy with a more distant background region. If the net counts were greater than three times the background error, we considered this to be a detection; otherwise we used three times the background error as the upper limit. The latter was the case for all seven cases.

If the single β model did not give a satisfactory fit we added the second β model as described in Croston et al. (2008a), so that we could describe the galaxy and cluster contributions separately and exclude the galaxy luminosity. In this model, the line-of-sight sum of the gas densities in the two components is given by

$$n(r) = n_0\left[\left(1 + (\frac{r}{r_{c,in}})^2\right)^{-3\beta_{in}/2} + N\left(1 + (\frac{r}{r_c})^2\right)^{-3\beta/2}\right] \tag{2}$$

where N is the relative normalisation of the two beta models and the subscript in refers to the inner (galaxy) model.

The surface brightness profile is then

$$S(R) \propto \int_{-\infty}^{\infty} n^2(l, R)dl \tag{3}$$

where the radius $r = \sqrt{l^2 + R^2}$, and l is the distance along the line of sight.

Since we are assuming the clusters and groups to be at least approximately relaxed, we limited β for the outer (ICM) model to the range 0.3 to 1.2 and r_c to a minimum of 1 kpc. We allowed more freedom in the parameters for the inner model, which describes the

---

[7] http://ned.ipac.caltech.edu/

host galaxy, since the galaxy is ellipsoidal rather than spherical and could be at any orientation to the line of sight.

The goodness-of-fit and ICM β model parameters are shown in Table 3, and Table 4 gives the inner beta model parameters for the sources where the galaxy emission was discernible. The distributions of β and r_c for the ICM model are shown in Figure 2. Except for a few high values, the values of β are mostly lower than the values of typical clusters, as is expected for less rich environments (e.g. Mulchaey 2000). The overall median β for the z0.1 sample is 0.47, close to the value of 0.5 expected for groups. The ERA sample also has a median of 0.47, showing consistency between the two samples.

There are eight sources with high values of β compared with the rest of the sample and six sources with a very low core radius. 3C 442A and PKS 0915−11 (Hyd A) contain interacting galaxies resulting in shocks propagating through the ICM. The disturbance is clearly visible in the surface brightness profiles. Both profiles contain sufficient counts to show that the outer ICM is well modelled. The other sources have very little emission detected beyond the host galaxy and so their models are poorly constrained. The profiles of the environments with high βs have emission visible beyond the host, but because there are few bins the profiles look flat and wide, and this is reflected in the model parameters. The outer emission of those sources with low core radii have the opposite problem, with the outer profile merging smoothly with that of the host galaxy so they are hard to differentiate.

For some of the inner β models, it was difficult to differentiate between the point source and the galaxy, and consequently some of the galaxy βs are very high. However, as we only wished to model the shapes in order to exclude them from the luminosity calculation, we did not expect this to be of concern provided the profile shape was well modelled. We tested this assumption using the sources with the two highest galaxy βs — 3C 98 and PKS 1559+02. We fixed the galaxy βs at the median value of 0.95, refitted the surface brightness profiles and recalculated the luminosities. They were both consistent with the luminosities calculated using the high values of β.

Because the *Chandra* blank sky files may not model the background accurately, we looked for systematic differences between the profiles made using double and single background subtraction. All the single subtraction sources have a large number of counts and well-defined profiles, and the β model parameters cover a similar range to those of the double subtraction sources. All except PKS 1648+05 (Her A) are towards the low end of the redshift range, so would be expected to cover the chip if the environment was relatively rich and/or the observation long.

Luminosity within the R_{500} overdensity radius was calculated by integrating the ICM β model profile using counts to flux conversion factors generated from the *apec* model. The β model profile was extrapolated to R_{500} using the $R - T$ relationship from Arnaud et al. (2005):

$$R_{500} = h(z)^{-1} B_{500} \left(\frac{kT}{5}\right)^{\beta} \tag{4}$$

where

$$h^2(z) = \Omega_m (1 + z)^3 + \Omega_\Lambda \tag{5}$$

We calculated a luminosity for each sample of the output of the MCMC code, which provided us with a posterior probability distribution function over luminosity, marginalized over all other parameters. We used the median rather than the mean of the posterior probability distribution function as our luminosity estimate
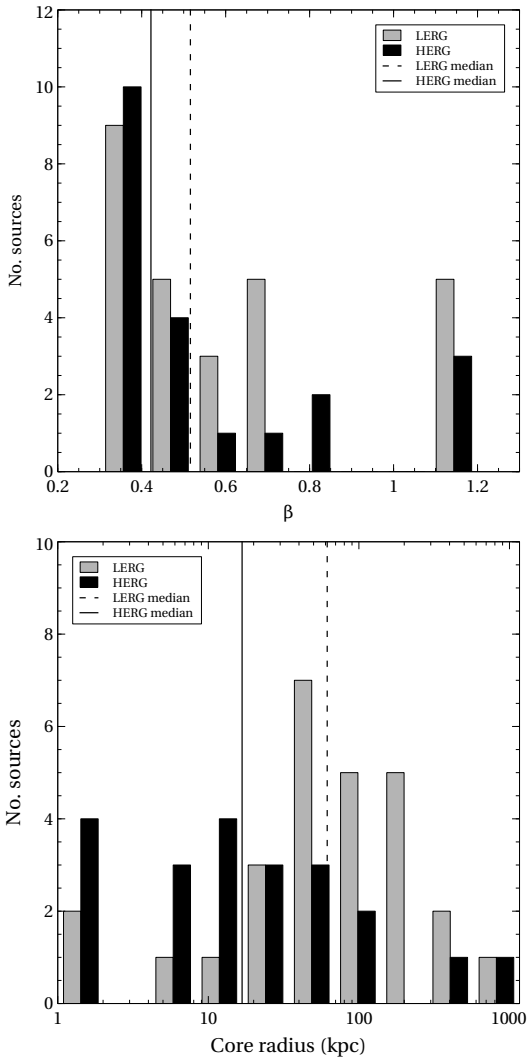
Figure 2. Distribution of the β model parameters for the z0.1 sample; β (above) and core radius (below). The LERGs are grey and the HERGs black. Dashed lines show the LERG medians and solid lines the HERG medians.

because the distributions were skewed for the fainter sources. Our quoted uncertainties on the luminosity are credible intervals defined on this one-dimensional posterior probability distribution function such that 68 per cent of the probability is contained in the smallest luminosity range. The luminosity uncertainties take into account the (in some cases large) uncertainties on β and r_c.

If the cluster emission extended beyond the chip, we could use only the *Chandra* blank sky datasets for the background subtraction. The lower energy background varies from field to field and the background is known to change with time (Markevitch et al. 2003) so the *Chandra* background for a given source may not be accurate. We checked how well on average the *Chandra* backgrounds modelled the true background by comparing their count rates with those of our source datasets using a chip lying beyond the maximum detected radius of the cluster emission. When the source was centred on the S3 chip, we compared background count rates on the I2 chip, and when it was centred on the I3 chip, we compared background rates on the S2 chip. We then increased the errors on the luminosity using the standard deviation of the differences (14.8 per cent and 8.5 per cent respectively).

Luminosity upper limits were calculated within the median

Table 3. Radial profile modeling - ICM (outer) β model

Source	Model[a], Method[b]	R_{det} kpc	Counts[c,d]	χ^2/dof	β[e,f]	r_c kpc
3C 28	$d\beta$, dsub	1432	14810	74/15	0.67 (0.55–0.85)	340.12 (253.47–437.35)
3C 31	$d\beta$, dsub	203	10827	104/62	0.30 (0.30–1.50)	39.34 (27.73–256.55)
3C 33	$d\beta$, dsub	113	2770	3.2/8	0.76 (0.30–1.20)	16.76 (1.46–112.81)
3C 35	$s\beta$, dsub	221	218	3.5/5	1.17 (0.30–1.20)	134.53 (2.08–384.43)
3C 66B	$d\beta$, dsub	282	13788	13/14	0.35 (0.31–0.37)	46.91 (33.33–59.22)
3C 76.1	$s\beta$, dsub	95	117	0.6/2	0.46 (0.30–1.20)	9.84 (0.82–64.56)
3C 98	$d\beta$, dsub	121	1380	1.4/8	0.42 (0.30–1.20)	1.79 (1.00–58.13)
3C 192	$s\beta$, dsub	170	191	1.1/3	0.41 (0.30–0.91)	1.02 (1.00–10.63)
3C 219	$s\beta$, dsub	726	2251	42266	0.40 (0.31–0.59)	28.13 (4.71–90.95)
3C 236	$d\beta$, dsub	359	1057	4.2/7	0.39 (0.30–1.20)	26.23 (5.84–358.57)
3C 285	$d\beta$, dsub	368	1521	4.1/9	0.36 (0.32–0.70)	14.63 (5.98–82.47)
3C 293	$d\beta$, dsub	104	2421	1.4/7	0.69 (0.47–1.20)	5.67 (2.29–13.20)
3C 296	$d\beta$, ssub	>147	6862	6.4/19	0.70 (0.30–1.20)	188.61 (58.28–338.58)
3C 303	$s\beta$, dsub	366	2510	3.7/9	0.51 (0.44–0.70)	1.23 (1.00–10.28)
3C 305	u/l		<797		*0.47*	*40.39*
3C 310	$d\beta$, ssub	>465	9456	126/20	0.50 (0.46–0.54)	41.34 (32.67–53.09)
3C 321	$d\beta$, dsub	87	843	6.8/8	1.19 (0.31–1.20)	30.56 (5.64–55.80)
3C 326	$d\beta$, dsub	328	321	0.2/5	1.11 (0.30–1.20)	738.42 (10.65–1670.72)
3C 338	$d\beta$, ssub	>364	363864	1595/39	0.63 (0.61–0.65)	91.37 (85.01–94.86)
3C 346	$d\beta$, dsub	411	5079	18/4	0.41 (0.33–0.64)	43.51 (19.53–102.90)
3C 386	$s\beta$, dsub	93	384	2.9/3	0.37 (0.30–0.52)	1.01 (1.00–4.17)
3C 388	$d\beta$, ssub	>667	8149	45/18	0.52 (0.49–0.56)	40.39 (31.04–52.38)
3C 390.3	$d\beta$, ssub	>294	12647	65/12	0.40 (0.37–0.42)	13.81 (7.33–21.18)
3C 433	$d\beta$, dsub	323	3058	42289	1.09 (0.30–1.20)	310.27 (3.75–593.38)
3C 442A	$d\beta$, ssub	>311	6344	44/14	1.11 (0.58–1.20)	212.86 (101.64–251.01)
3C 449	$d\beta$, ssub	>119	10260	17/14	0.36 (0.33–0.40)	18.76 (13.11–28.43)
3C 452	$d\beta$, dsub	300	3202	7.4/12	0.74 (0.42–1.20)	64.33 (21.33–125.26)
3C 465	$d\beta$, ssub	>240	37631	18/18	0.53 (0.45–0.74)	155.90 (122.39–216.79)
4C 73.08	$s\beta$, dsub	167	624	8.9/4	0.42 (0.31–1.20)	1.01 (1.00–68.33)
DA 240	u/l		<433		*0.47*	*40.89*
NGC 6109	$d\beta$, dsub	131	710	4.5/8	1.20 (0.30–1.20)	167.46 (24.80–579.03)
NGC 6251	$d\beta$, ssub	>220	2084	20/18	0.33 (0.30–0.55)	54.90 (27.11–152.64)
NGC 7385	u/l		<1122		*0.47*	*40.89*
PKS 0034-01	u/l		<254		*0.47*	*40.90*
PKS 0038+09	$d\beta$, dsub	231	1238	43/9	0.78 (0.30–1.20)	71.48 (3.96–975.12)
PKS 0043-42	$s\beta$, dsub	413	576	7.8/5	0.34 (0.30–0.44)	1.03 (1.00–20.71)
PKS 0213-13	$s\beta$, dsub	126	1244	2.9/5	0.63 (0.30–1.20)	18.75 (4.09–81.14)
PKS 0349-27	$d\beta$, dsub	310	839	1.0/8	0.30 (0.30–1.50)	97.58 (39.93–1256.53)
PKS 0404+03	u/l		<122		*0.47*	*40.89*
PKS 0442-28	u/l		<126		*0.47*	*40.87*
PKS 0620-52	$d\beta$, ssub	>368	8843	2.5/10	0.42 (0.37–0.48)	61.59 (41.52–89.35)
PKS 0625-35	$d\beta$, ssub	>365	5280	19/10	0.36 (0.31–0.67)	40.38 (16.00–168.57)
PKS 0625-53	$d\beta$, ssub	>412	28390	11/11	0.48 (0.43–0.53)	105.59 (85.04–132.56)
PKS 0806-10	u/l		<161		*0.47*	*40.99*
PKS 0915-11	$d\beta$, ssub	>315	661760	1339/16	1.20 (0.68–1.20)	302.13 (142.07–417.93)
PKS 0945+07	$d\beta$, dsub	318	4404	10/13	0.40 (0.31–0.95)	7.04 (2.04–50.06)
PKS 1559+02	$d\beta$, dsub	564	1255	8.7/11	0.30 (0.30–1.20)	6.85 (1.00–1807.76)
PKS 1648+05	$d\beta$, ssub	>859	25027	538/16	0.63 (0.60–0.65)	93.97 (85.55–101.46)
PKS 1733-56	$d\beta$, dsub	492	4055	51/9	1.16 (0.30–1.20)	1165.77 (18.33–1813.91)
PKS 1839-48	$d\beta$, dsub	547	6934	21/14	0.66 (0.58–0.75)	191.20 (156.78–239.38)
PKS 1949+02	$d\beta$, dsub	252	2435	7.5/8	0.38 (0.30–1.20)	7.36 (1.81–111.99)
PKS 1954-55	$d\beta$, ssub	>415	7689	25/17	0.36 (0.33–0.41)	30.12 (13.96–51.95)
PKS 2211-17	$d\beta$, dsub	784	31037	362/16	0.72 (0.69–0.74)	81.51 (76.04–87.60)
PKS 2221-02	$d\beta$, dsub	240	8775	22/16	0.35 (0.30–1.00)	16.56 (7.20–105.59)
PKS 2356-61	$d\beta$, dsub	526	1791	1.8/14	0.42 (0.30–1.20)	56.34 (12.69–279.51)

[a] Single or double β model, or upper limit. [b] Single or double background subtraction. [c] Upper limits are counts within the median R_{500}. [d] Counts for *XMM-Newton* sources are for the pn camera only. [e] Values for β and core radius r_c are best fit parameters. Ranges are the Bayesian credible intervals. [f] Italics indicate median values used for sources with low counts.

Table 4. Radial profile modeling - host galaxy (inner) β model

Source	χ^2/dof	$\beta^{a,b}$	r_c kpc
3C 28	74/13	0.74 (0.62–0.90)	36.80 (27.05–47.40)
3C 31	104/62	0.79 (0.51–1.02)	1.32 (0.32–1.85)
3C 33	4.4/6	1.20 (0.85–2.00)	0.99 (0.55–2.01)
3C 66B	42351	2.86 (1.09–3.00)	10.19 (4.35–12.24)
3C 98	1.4/6	2.92 (0.77–3.00)	0.86 (0.20–1.28)
3C 236	4.2/5	1.20 (0.91–2.99)	2.45 (1.60–6.36)
3C 285	4.3/7	1.12 (1.00–3.00)	0.79 (0.49–4.11)
3C 293	1.6/5	0.98 (0.49–1.20)	0.66 (0.14–1.23)
3C 296	7.1/17	0.64 (0.59–0.71)	0.66 (0.48–0.88)
3C 310	128/22	0.83 (0.56–2.00)	2.90 (1.67–8.93)
3C 321	7.2/6	2.64 (1.07–3.50)	6.12 (2.79–8.33)
3C 326	0.2/3	0.95 (0.70–1.50)	10.80 (4.21–35.56)
3C 338	1625/37	0.58 (0.56–0.61)	11.94 (11.07–12.86)
3C 346	18/5	1.20 (1.20–1.20)	2.54 (1.00–4.44)
3C 388	48/16	1.26 (0.79–2.50)	7.47 (4.26–17.71)
3C 390.3	65/10	1.07 (0.96–1.25)	5.35 (4.51–6.43)
3C 433	12.3/8	1.14 (0.50–1.20)	10.85 (1.49–16.84)
3C 442A	44.5/12	0.53 (0.41–0.90)	6.15 (3.01–16.30)
3C 449	17.3/12	0.95 (0.72–2.14)	0.96 (0.55–2.21)
3C 452	7.5/10	1.52 (0.96–3.00)	1.29 (0.61–2.55)
3C 465	20/16	0.66 (0.61–0.73)	0.80 (0.60–1.12)
NGC 6109	4.5/6	0.70 (0.47–1.00)	1.21 (0.23–3.26)
NGC 6251	18/11	0.71 (0.57–0.88)	0.63 (0.28–1.08)
PKS 0038+09	43/7	2.50 (0.96–2.50)	19.46 (8.19–25.83)
PKS 0349-27	1.1/6	2.13 (0.45–2.50)	11.05 (1.59–23.59)
PKS 0620-52	2.7/8	0.77 (0.61–1.12)	0.73 (0.22–0.97)
PKS 0625-35	21/8	0.80 (0.66–0.99)	2.97 (1.93–4.32)
PKS 0625-53	3.4/6	0.65 (0.39–0.80)	0.53 (0.11–1.29)
PKS 0915-11	237/15	0.89 (0.56–1.44)	30.25 (21.30–40.56)
PKS 0945+07	11/11	0.86 (0.71–1.40)	0.60 (0.37–1.52)
PKS 1559+02	9.0/9	2.99 (1.14–3.00)	3.25 (1.28–3.75)
PKS 1648+05	538/14	2.32 (1.65–3.00)	19.96 (15.00–26.27)
PKS 1733-56	51/7	0.56 (0.30–1.27)	2.47 (0.18–10.68)
PKS 1839-48	21/12	0.79 (0.50–1.49)	3.03 (0.81–7.17)
PKS 1949+02	63/9	0.88 (0.61–1.94)	0.65 (0.36–1.32)
PKS 1954-55	14/14	0.61 (0.47–1.14)	2.55 (1.78–8.68)
PKS 2211-17	363/14	2.49 (1.58–2.50)	15.23 (10.20–17.05)
PKS 2221-02	28/14	1.15 (0.99–1.34)	1.48 (1.16–1.84)
PKS 2356-61	1.9/12	1.16 (0.64–2.00)	3.92 (1.14–9.38)

[a] Values for β and core radius r_c are best fit parameters. Ranges are the Bayesian credible intervals. [b] Italics indicate median values used for sources with low counts.

R_{500} (533 kpc), using the median β and r_c for the profile shapes and the count rate upper limits for the normalisations.

Table 5 contains the bolometric X-ray luminosities for each source: within the maximum detection radius; within R_{500}; and scaled by $h^{-1}(z)$ to correct for the critical density evolution. Figure 3 shows the luminosity distribution; it can be seen that the most luminous environments are occupied by LERGs.

The sources with emission extending beyond the chip have luminosities from 0.4×10^{43} to 61×10^{43} erg s^{-1}, so cover most of the luminosity range. Since their emission is so extensive, it is to be expected that they tend to be high luminosity. Five of the ten clusters with luminosity greater than 10^{44} erg s^{-1} are among this group, and they include four of the five most luminous clusters.

We also wished to gain some idea of the central conditions of the radio galaxy environments so we calculated the environment density at a radius of $0.1R_{500}$; for all but two of sources this was not much larger than the host galaxy radius and so was the closest

radius to the source that we could measure the density. We used the method described in Birkinshaw & Worrell (1993):

$$\mathscr{A} = \frac{\int n_e n_p dV}{4\pi d\Omega D_L^2} \tag{6}$$

where $\mathscr{A}$ is the distance-normalised volume emission measure of the atmosphere per unit solid angle, n_e and n_p are the electron and proton densities, dV is a cylindrical volume element subtending a solid angle $d\Omega$ to the observer and D_L is the luminosity distance to the source. We assumed an electron-proton ratio of 1.18.

We obtained the emission measure normalisation from the normalisation of the *apec* model used in the spectral analysis (see below). We then calculated the electron density at $0.1R_{500}$ for each sample in the MCMC code output, using the same method that we used for the luminosity calculations (see above). The uncertainties were also derived in the same manner. The densities are included in Table 5.

Table 5. ICM X-ray luminosity and electron density

Source	$L_X(bol)$ $\times 10^{43}$ erg s^{-1} within D_{rad}	$R_{500}{}^a$ kpc	$L_X(bol)$ $\times 10^{43}$ erg s^{-1} within R_{500}	$h(z)^{-1}L_X(bol)$ $\times 10^{43}$ erg s^{-1} within R_{500}	n_e m^{-3} at $0.1R_{500}$
3C 28	$111.300^{+2.329}_{-2.118}$	1175	$107.400^{+1.791}_{-1.753}$	97.558	3667^{+27}_{-27}
3C 31	$0.626^{+0.056}_{-0.033}$	549	$2.013^{+0.326}_{-0.141}$	1.998	686^{+30}_{-30}
3C 33	$0.489^{+0.017}_{-0.021}$	458	$0.491^{+0.020}_{-0.027}$	0.478	179^{+84}_{-75}
3C 35	$0.248^{+0.086}_{-0.101}$	420	$0.302^{+0.127}_{-0.174}$	0.293	772^{+105}_{-94}
3C 66B	$1.444^{+0.030}_{-0.030}$	601	$3.173^{+0.095}_{-0.119}$	3.143	936^{+10}_{-10}
3C 76.1	$0.042^{+0.020}_{-0.025}$	341	$0.080^{+0.052}_{-0.079}$	0.079	573^{+163}_{-131}
3C 98	$0.063^{+0.013}_{-0.016}$	330	$0.066^{+0.020}_{-0.021}$	0.065	407^{+212}_{-197}
3C 192	$0.106^{+0.032}_{-0.035}$	376	$0.155^{+0.057}_{-0.067}$	0.151	650^{+111}_{-72}
3C 219	$6.866^{+0.869}_{-1.027}$	501	$5.193^{+0.577}_{-0.513}$	4.770	2708^{+165}_{-159}
3C 236	$0.679^{+0.083}_{-0.111}$	475	$0.693^{+0.095}_{-0.138}$	0.661	484^{+164}_{-121}
3C 285	$0.522^{+0.115}_{-0.096}$	409	$0.559^{+0.135}_{-0.111}$	0.539	881^{+62}_{-64}
3C 293	$0.048^{+0.003}_{-0.004}$	373	$0.049^{+0.003}_{-0.005}$	0.048	290^{+86}_{-122}
3C 296	$0.229^{+0.034}_{-0.034}$	569	$0.567^{+0.128}_{-0.168}$	0.560	490^{+18}_{-17}
3C 303	$0.749^{+0.113}_{-0.113}$	397	$0.757^{+0.115}_{-0.114}$	0.707	1547^{+150}_{-107}
3C 305		*533*	<0.078	<0.077	<201
3C 310	$2.997^{+0.448}_{-0.448}$	623	$3.340^{+0.501}_{-0.501}$	3.258	1940^{+27}_{-27}
3C 321	$0.208^{+0.010}_{-0.010}$	388	$0.211^{+0.011}_{-0.013}$	0.202	604^{+108}_{-88}
3C 326	$2.000^{+1.182}_{-1.935}$	617	$4.650^{+3.966}_{-4.585}$	4.458	216^{+28}_{-17}
3C 338	$40.140^{+5.941}_{-5.941}$	1041	$49.440^{+7.319}_{-7.320}$	48.746	3538^{+4}_{-4}
3C 346	$7.474^{+0.608}_{-0.915}$	731	$10.810^{+1.443}_{-2.280}$	9.991	2090^{+46}_{-55}
3C 386	$0.033^{+0.007}_{-0.008}$	450	$0.104^{+0.034}_{-0.041}$	0.103	345^{+39}_{-36}
3C 388	$13.050^{+1.138}_{-1.141}$	866	$14.040^{+1.240}_{-1.230}$	13.450	2538^{+25}_{-24}
3C 390.3	$3.161^{+0.469}_{-0.469}$	662	$4.262^{+0.637}_{-0.636}$	4.152	1223^{+23}_{-25}
3C 433	$0.235^{+0.097}_{-0.063}$	409	$0.240^{+0.117}_{-0.069}$	0.229	485^{+54}_{-168}
3C 442A	$1.129^{+0.101}_{-0.101}$	564	$1.283^{+0.119}_{-0.121}$	1.268	658^{+17}_{-14}
3C 449	$0.414^{+0.062}_{-0.062}$	583	$1.752^{+0.283}_{-0.280}$	1.738	911^{+14}_{-15}
3C 452	$0.768^{+0.045}_{-0.054}$	496	$0.788^{+0.052}_{-0.070}$	0.759	1250^{+66}_{-57}
3C 465	$3.465^{+0.514}_{-0.514}$	1016	$8.903^{+1.541}_{-1.541}$	8.780	554^{+4}_{-4}
4C 73.08	$0.036^{+0.017}_{-0.025}$	512	$0.049^{+0.029}_{-0.042}$	0.048	258^{+154}_{-90}
DA 240		*533*	<0.083	<0.081	<290
NGC 6109	$0.136^{+0.036}_{-0.052}$	412	$0.239^{+0.105}_{-0.154}$	0.236	577^{+41}_{-41}
NGC 6251	$0.183^{+0.027}_{-0.027}$	523	$0.444^{+0.074}_{-0.071}$	0.439	348^{+17}_{-16}
NGC 7385		*533*	<0.064	<0.063	<256
PKS 0034-01		*533*	<0.063	<0.061	<264
PKS 0038+09	$2.418^{+0.458}_{-0.446}$	566	$2.652^{+0.596}_{-0.776}$	2.418	1754^{+504}_{-354}
PKS 0043-42	$1.018^{+0.198}_{-0.275}$	543	$1.317^{+0.282}_{-0.397}$	1.246	863^{+61}_{-55}
PKS 0213-13	$0.184^{+0.060}_{-0.075}$	375	$0.205^{+0.080}_{-0.101}$	0.190	1193^{+316}_{-237}
PKS 0349-27	$0.280^{+0.132}_{-0.189}$	392	$0.332^{+0.176}_{-0.246}$	0.322	270^{+36}_{-69}
PKS 0404+03		*533*	<0.268	<0.257	<549
PKS 0442-28		*533*	<0.273	<0.254	<304
PKS 0620-52	$3.941^{+0.590}_{-0.589}$	768	$6.742^{+1.047}_{-1.036}$	6.585	1261^{+18}_{-18}
PKS 0625-35	$3.150^{+0.477}_{-0.477}$	872	$6.334^{+1.067}_{-1.053}$	6.176	883^{+24}_{-27}
PKS 0625-53	$22.260^{+1.912}_{-1.917}$	1287	$42.610^{+3.928}_{-3.945}$	41.560	1609^{+16}_{-15}
PKS 0806-10		*533*	<0.206	<0.195	<482
PKS 0915-11	$54.560^{+8.075}_{-8.075}$	851	$61.800^{+9.146}_{-9.147}$	60.248	5140^{+8}_{-11}
PKS 0945+07	$1.608^{+0.128}_{-0.173}$	562	$1.790^{+0.206}_{-0.313}$	1.719	903^{+89}_{-94}
PKS 1559+02	$1.041^{+0.233}_{-0.441}$	329	$0.790^{+0.160}_{-0.180}$	0.752	803^{+348}_{-110}
PKS 1648+05	$57.830^{+8.571}_{-8.570}$	995	$58.620^{+8.689}_{-8.687}$	54.375	4976^{+24}_{-29}
PKS 1733-56	$0.826^{+0.349}_{-0.604}$	506	$0.842^{+0.365}_{-0.618}$	0.803	680^{+35}_{-51}
PKS 1839-48	$18.730^{+0.391}_{-0.445}$	1156	$23.640^{+0.665}_{-0.825}$	22.424	1570^{+26}_{-24}
PKS 1949+02	$0.217^{+0.041}_{-0.061}$	411	$0.259^{+0.068}_{-0.100}$	0.252	610^{+65}_{-70}
PKS 1954-55	$4.496^{+0.109}_{-0.109}$	785	$7.767^{+0.323}_{-0.310}$	7.560	1262^{+23}_{-21}
PKS 2211-17	$28.360^{+0.232}_{-0.262}$	916	$28.640^{+0.238}_{-0.265}$	26.593	4397^{+23}_{-26}
PKS 2221-02	$1.169^{+0.056}_{-0.086}$	450	$1.428^{+0.128}_{-0.222}$	1.391	782^{+34}_{-38}
PKS 2356-61	$1.452^{+0.308}_{-0.424}$	465	$1.383^{+0.252}_{-0.373}$	1.321	1049^{+152}_{-120}

^{a} Italics indicate median value used for sources with low counts.
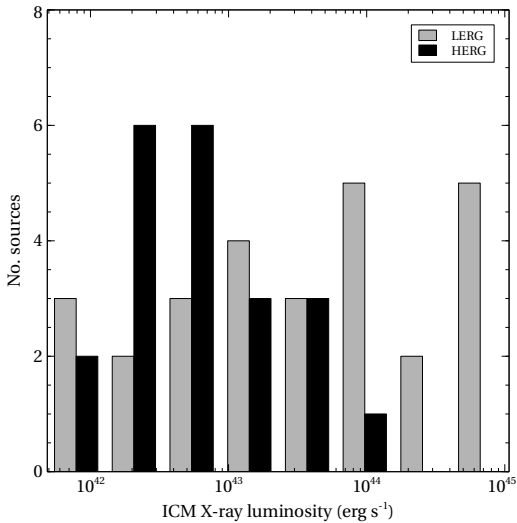
Figure 3. ICM X-ray luminosity distribution for the z0.1 sample, separated into excitation classes (upper limits excluded). Symbols as in Figure 2.

4.2 Spectral analysis

When there were sufficient counts, we obtained the ICM temperature from spectral analysis. We used the XSPEC package, using the *apec* model for the thermal bremsstrahlung from the ICM and the *wabs* photo-electric absorption model to take account of Galactic absorption. We reduced the energy range to 0.5 to 5.0 keV to exclude the PSF-scattered high energy emission from the nucleus and, where possible, we used a double subtraction method similar to that used for the *XMM-Newton* temperatures in I13, using the following steps:

(i) Generate the spectrum for a background region beyond the maximum detected radius with *specextract*, using the *Chandra* blank sky files or *XMM-Newton* closed filter files for the spectrum background file. Then scale the blank sky background spectrum to match the source file count rate (see Section 3.1);

(ii) Fit models to this background region using a power law with index 1.41 to model the extragalactic component of the X-ray background (Lumb et al. 2002), with Galactic absorption (*wabs(power)*). We added local thermal models (*apec*) for the Milky Way emission and local hot bubble as appropriate;

(iii) Generate the spectrum for the ICM using an annulus from where the ICM dominates over the PSF and host galaxy emission out to the maximum detection radius. Again, the *Chandra* blank sky files or *XMM-Newton* closed filter files are used for the spectrum background and the blank sky spectrum is scaled to match the source file count rate;

(iv) Scale the normalisations of the background model elements to match the source region area;

(v) Model the source bremsstrahlung using *wabs(apec)*, with the elements of the background model as fixed parameters. When possible, we left the metallicity as a free parameter. If it did not converge to a reasonable value (0.15 to 0.6 solar – Balestra et al. 2007), or had errors larger than this range, we used 0.3 solar.

In some sources, the *Chandra* blank sky files matched the background from the source observation sufficiently well that there were very few counts left after the background subtraction. In these cases, we used the same method as I13, using single subtraction
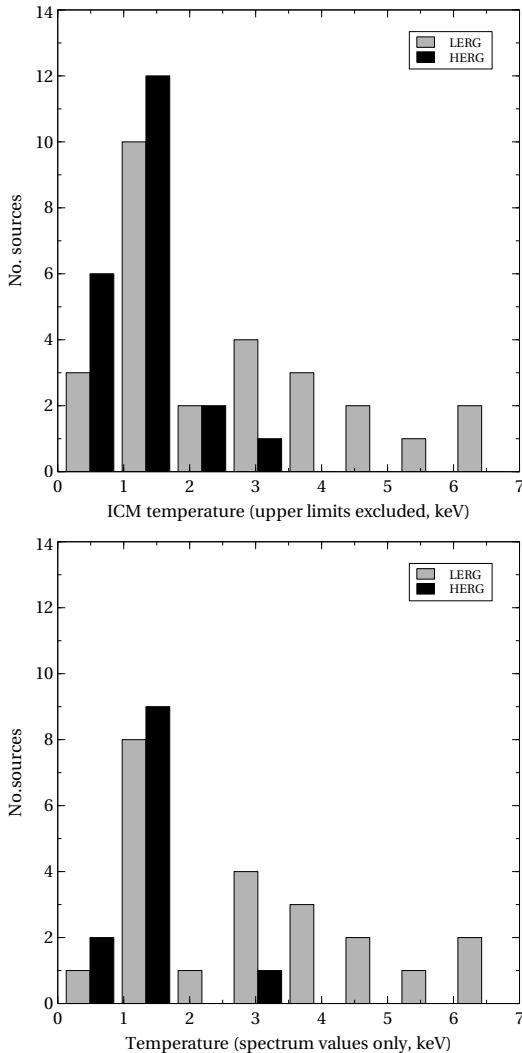
Figure 4. ICM temperature distribution for the z0.1 sample, separated into excitation classes (upper limits excluded). The upper histogram includes all sources; the lower histogram shows only those with temperatures obtained by spectral analysis. Symbols as in Figure 2.

with a region from outside the maximum detected radius as the background for the spectrum.

If the source emission was so extensive that there was no region of the source observation that could be used for background, we could not use double subtraction. In this case, single subtraction using the blank sky files as background was the only method available. In addition to the ICM emission, the cosmic ray background and local thermal emission were modelled as in the double subtraction method, but were left as free parameters.

When there were sufficient counts, we generated a temperature profile and selected an annulus for the ICM temperature across a wide range of stable results, excluding the cool core if present. Otherwise we obtained temperatures for a range of annuli, looking for the lowest χ^2.

For 3C 31 and 3C 66B, we also excluded the 1.4 to 1.6 keV energy band from the spectrum to remove the *XMM-Newton* 1.5 keV instrumental aluminium fluorescence line (Freyberg et al. 2002).

The spectra for 18 sources had insufficient counts for modelling the spectrum. For these sources we extracted a spectrum to the maximum detected radius and estimated the temperature in the

same way as in I13, using the counts from the β model to estimate luminosity from the *apec* model, and then using the scaling relation of Pratt et al. (2009) to estimate the temperature. This was used to estimate R_{500}, and the process was iterated until we obtained a stable temperature. We used the same process for the seven sources without a β model fit, using the 3σ upper limit on the counts to estimate the starting luminosity.

The distribution of temperatures is shown in Figure 4, and Table 6 contains the inner and outer radii of the annuli, the temperatures of the sources and the χ^2 for the temperatures obtained by spectral analysis. The temperatures range from 0.65 to 6.8 keV – a similar range to the ERA sample – and are for the most part typical of groups and poor clusters. The temperatures for the sources where the emission extended beyond the chip included the highest temperature (6.8 keV), but otherwise ranged from 1.38 keV to 4.43 keV, not concentrated in or dominating any temperature range. Although both the distributions of both types of radio galaxy peak at low temperatures, the LERGs have a wider range of temperatures with the top of the range being occupied exclusively by LERGs.

5 RESULTS AND DISCUSSION

5.1 Radio galaxy environments

5.1.1 z0.1 sample results

We first compared radio and ICM luminosities for the z0.1 sample, to see if the results differed from those found for the ERA sample. As can be seen from Figure 5 (left), the HERG subsample appears to cluster in the lower, central region of the plot, while the LERG sub-sample forms a diagonal across the plot. Since there is a strong correlation between radio luminosity and redshift from the Malmquist bias and the lack of high luminosity local sources (see Figure 1), we used partial correlation Kendall's τ tests (Akritas & Siebert 1996) to look for correlations between the radio and ICM luminosities in the presence of a dependency on redshift, and found a weak correlation for the full sample, a strong correlation for the LERG sub-sample ($> 3\sigma$) and no correlation for the HERGs (Table 7). These results agree with those found with the ERA sample at $z \sim 0.5$, and, as discussed in Section 1, by Best (2004); Hardcastle (2004); Belsole et al. (2007); Gendre et al. (2013).

Because the sources are relatively close, the maximum detected radius is on average only half of R_{500}. Consequently, the beta models needed to be extrapolated to calculate the luminosities for all but ten of the sources. We therefore also calculated the luminosity for each source within $0.5R_{500}$ (which was within the maximum detected radius for 80 per cent of the sources) to check that the statistical results were similar. This gave similar results for the partial correlation tests between the sub-samples ($> 3\sigma$ for the LERGS, no correlation for the HERGs), implying that the extrapolation to R_{500} does not have a significant effect.

We also checked the LERG results for a sub-sample with $z > 0.03$, removing the bulk of the redshift dependence, which gave a weaker correlation ($> 2\sigma$). This was to be expected, since the scatter is proportionally greater over the reduced luminosity range.

For the FRI and FRII sub-samples in Figure 5 (right), there appears to be a correlation between radio and ICM luminosity for both sub-samples, and this is confirmed by the partial correlation tests (Table 7) ($> 2.5\sigma$ for both sub-samples). Since the FRI and FRII sub-samples contain both HERGs and LERGs, one would expect their correlation strengths to lie between those of the HERGs and LERGs, and this is the case.

Table 8. Tests for differences in sample median ICM luminosities, using the Peto-Prentice two-sample test

Sample	Sub-sample	N1	N2	statistic	p
Full	All	55	26	1.8760	0.0607
	HERG	25	15	3.6860	0.0002
	LERG	30	11	0.1640	0.8696
Matched	HERG	22	7	2.2800	0.0226
	LERG	20	7	1.5340	0.1249

N1 and N2 are the sizes of the samples being compared; p is probability under the null hypothesis.

5.1.2 Combined z0.1 and ERA samples

Figure 6 shows the radio vs ICM luminosities for the combined ERA and $z \sim 0.1$ samples for the LERGs (left) and HERGs (right). Both of the LERG samples occupy the same diagonal across the plot, with a similar amount of scatter, and the partial correlation test gives a strong correlation ($> 4\sigma$). The HERGs show a much weaker correlation ($> 2\sigma$) – looking at Figure 6 the correlation appears to come from the absence of low ICM luminosities for the ERA sources. See Section 5.1.3 below for a discussion of the lack of sources in this region.

The z0.1 and ERA samples cover different ranges of radio luminosity. We therefore checked our result using sub-samples matched in luminosity ranges: $5 \times 10^{24} - 5 \times 10^{26}$ W Hz^{-1} sr^{-1} for the LERGs and $3 \times 10^{25} - 3 \times 10^{26}$ W Hz^{-1} sr^{-1} for the HERGs (Table 7). In these sub-samples, the strong LERG $L_X - L_R$ correlation is still present, but since the high radio luminosity HERGs are no longer in the sample, the partial correlation Kendall's τ test now showed no correlation for the HERGs. The reduced ERA samples are small and contain upper limits on the ICM luminosities so may affect the accuracy of the statistics; nevertheless, the difference between the HERG and LERG results in both the complete and matched samples is striking.

5.1.3 Redshift evolution

Looking at Figure 7, there seems to be little difference between the LERG samples from the two epochs, suggesting that there has been no evolution of the environment since $z \sim 0.5$. The ERA HERG sample, however, occupies a narrower range of ICM luminosities than the z0.1 HERG sample, but with similar maximum values. This may indicate that there has been evolution of the HERG environments, as suggested by Harvanek et al. (2001) and Belsole et al. (2007).

We used Peto & Prentice generalised Wilcoxon tests (Feigelson & Nelson 1985) to look for differences in the median values of luminosity of the ERA and z0.1 LERG and HERG sub-samples (Table 8; the medians are shown in Figure 7). The tests showed no difference between the two LERG sub-samples, but a strong difference between the HERG sub-samples ($> 3\sigma$). We repeated the tests with the sub-samples matched in radio luminosity (Figure 8), and found the same but weaker trends.

We therefore have no evidence of evolution of the LERG population since $z \sim 0.5$, but for the HERGs, although the maximum environment richness of the HERG population in the matched samples is the same at both redshifts, there are HERGs in poorer envi-

Table 6. ICM temperatures

Source	Method	Annulus radii arcsec	Metallicity[a] $Z/Z_\odot$	Temperature keV	χ^2/dof[b]
3C 28	Spectrum	24.60-246	0.30	$6.61^{+0.59}_{-0.49}$	106/143
3C 31	Spectrum	60.00-600	0.30	$1.52^{+0.03}_{-0.03}$	2198/1430
3C 33	Estimate	2.46-98	0.30	$1.12^{+0.01}_{-0.02}$	
3C 35	Estimate	2.46-172	0.30	$0.97^{+0.10}_{-0.20}$	
3C 66B	Spectrum	50.00-600	$0.21^{+0.04}_{-0.03}$	$1.71^{+0.05}_{-0.04}$	711/691
3C 76.1	Estimate	2.46-147	0.30	$0.80^{+0.07}_{-0.12}$	
3C 98	Estimate	2.95-196	0.30	$0.62^{+0.04}_{-0.06}$	
3C 192	Estimate	1.48-147	0.30	$0.80^{+0.07}_{-0.12}$	
3C 219	Spectrum	4.92-172	0.15	$1.46^{+0.13}_{-0.14}$	36/28
3C 236	Estimate	2.46-196	0.30	$1.24^{+0.05}_{-0.08}$	
3C 285	Spectrum	34.40-172	0.30	$0.94^{+0.10}_{-0.22}$	22/17
3C 293	Spectrum	2.46-73	0.30	$0.78^{+0.06}_{-0.06}$	18/12
3C 296	Spectrum	19.68-147	0.15	$1.59^{+0.12}_{-0.12}$	45/54
3C 303	Spectrum	2.46-123	0.30	$0.94^{+0.09}_{-0.13}$	7.2/7
3C 305	Upper limit	9.84-147	0.30	< 0.65	
3C 310	Spectrum	9.84-246	$0.26^{+0.07}_{-0.06}$	$1.92^{+0.12}_{-0.13}$	135/134
3C 321	Estimate	2.46-49	0.30	$0.87^{+0.01}_{-0.02}$	
3C 326	Estimate	14.76-196	0.30	$1.94^{+0.40}_{-1.35}$	
3C 338	Spectrum	19.68-344	$0.44^{+0.04}_{-0.04}$	$4.63^{+0.08}_{-0.08}$	392/304
3C 346	Spectrum	2.46-98	0.30	$2.79^{+0.24}_{-0.21}$	111/94
3C 386	Spectrum	2.46-270	0.30	$1.05^{+0.18}_{-0.12}$	12/15
3C 388	Spectrum	9.84-344	$0.53^{+0.18}_{-0.15}$	$3.52^{+0.18}_{-0.15}$	141/167
3C 390.3	Estimate	2.46-270	0.30	$2.14^{+0.01}_{-0.01}$	
3C 433	Spectrum	9.84-147	0.30	$0.96^{+0.76}_{-0.27}$	6.8/10
3C 442A	Spectrum	14.76-319	$0.24^{+0.12}_{-0.09}$	$1.58^{+0.11}_{-0.17}$	75/85
3C 449	Spectrum	14.76-147	$0.33^{+0.09}_{-0.08}$	$1.66^{+0.06}_{-0.07}$	63/77
3C 452	Spectrum	9.84-147	0.30	$1.32^{+0.10}_{-0.08}$	45/46
3C 465	Spectrum	9.84-295	$0.36^{+0.09}_{-0.08}$	$4.43^{+0.26}_{-0.23}$	255/259
4C 73.08	Spectrum	14.76-147	0.30	$1.37^{+0.26}_{-0.18}$	8.3/8
DA 240	Upper limit	14.76-147	0.30	< 0.66	
NGC 6109	Estimate	9.84-221	0.30	$0.91^{+0.11}_{-0.24}$	
NGC 6251	Spectrum	34.44-246	0.30	$1.38^{+0.21}_{-0.03}$	30/25
NGC 7385	Upper limit	4.92-147	0.30	< 0.61	
PKS 0034-01	Upper limit	9.84-147	0.30	< 0.61	
PKS 0038+09	Estimate	2.46-73	0.30	$1.82^{+0.12}_{-0.18}$	
PKS 0043-42	Spectrum	2.46-196	$0.41^{+0.69}_{-0.69}$	$1.59^{+0.96}_{-0.33}$	1.2/6
PKS 0213-13	Estimate	4.92-49	0.30	$0.85^{+0.09}_{-0.15}$	
PKS 0349-27	Spectrum	2.95-246	0.30	$0.86^{+0.16}_{-0.20}$	15/13
PKS 0404+03	Upper limit	19.68-147	0.30	< 0.93	
PKS 0442-28	Upper limit	9.84-147	0.30	< 0.93	
PKS 0620-52	Spectrum	19.68-246	$0.46^{+0.41}_{-0.19}$	$2.76^{+1.10}_{-0.60}$	115/137
PKS 0625-35	Spectrum	4.92-246	0.30	$3.46^{+0.48}_{-0.31}$	64/83
PKS 0625-53	Spectrum	24.60-295	0.30	$6.84^{+0.38}_{-0.34}$	171/188
PKS 0806-10	Upper limit	19.68-147	0.30	< 0.86	
PKS 0915-11	Spectrum	2.46-246	$0.30^{+0.02}_{-0.02}$	$3.31^{+0.10}_{-0.11}$	399/301
PKS 0945+07	Estimate	2.46-196	0.30	$1.64^{+0.06}_{-0.10}$	
PKS 1559+02	Spectrum	4.92-221	0.30	$0.65^{+0.10}_{-0.18}$	15/25
PKS 1648+05	Spectrum	14.76-196	$0.24^{+0.11}_{-0.10}$	$4.29^{+0.11}_{-0.11}$	200/239
PKS 1733-56	Spectrum	9.84-196	0.30	$1.38^{+0.42}_{-0.08}$	22/20
PKS 1839-48	Spectrum	4.92-147	0.30	$5.95^{+0.80}_{-0.72}$	89/102
PKS 1949+02	Estimate	4.92-221	0.30	$0.93^{+0.07}_{-0.12}$	
PKS 1954-55	Spectrum	4.92-246	0.30	$2.89^{+0.22}_{-0.22}$	172/121
PKS 2211-17	Spectrum	24.60-196	0.30	$4.11^{+0.18}_{-0.18}$	165/134
PKS 2221-02	Spectrum	4.92-221	0.30	$1.09^{+0.60}_{-0.40}$	52/57
PKS 2356-61	Spectrum	4.92-196	0.30	$1.19^{+0.14}_{-0.20}$	17/15

[a] Metallicities without errors were used as fixed parameters. [b] For temperatures from spectral analysis.
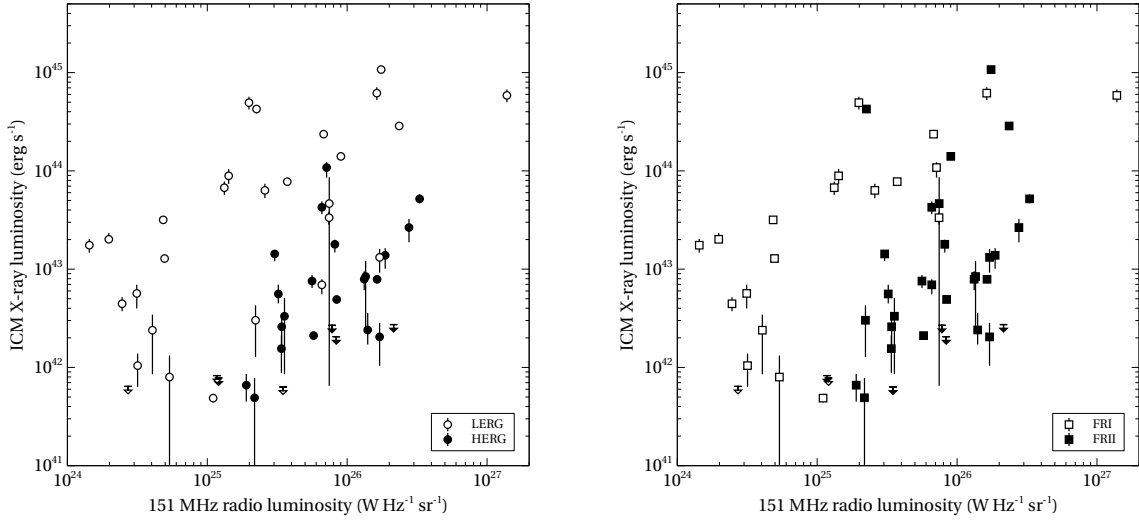
Figure 5. Radio luminosity vs ICM X-ray luminosity for the z0.1 sample, separated into excitation classes (left), and FRI and FRII galaxies (right). LERGs/FRIs are shown by empty symbols and HERGs/FRIIs by filled symbols. Corresponding upper limits are shown by empty and filled arrows.

Table 7. Partial correlation analysis results, using Generalized Kendall's τ correlation tests in the presence of a correlation with a third factor.

Sample	Sub-sample	N	τ/σ	p
Radio luminosity vs ICM luminosity, with a redshift correlation				
z0.1	All	55	2.62	0.0088
	HERG	25	1.68	0.0930
	LERG	30	3.39	0.0006
	FRI	22	2.96	0.0030
	FRII	33	2.91	0.0036
Radio luminosity vs ICM luminosity, with a redshift correlation				
0.03<z<0.2	All	46	2.37	0.0178
	HERG	25	1.68	0.0930
	LERG	21	2.72	0.0066
Radio luminosity vs ICM luminosity, with a redshift correlation				
z0.1 and ERA	All	81	4.09	0.0001
	HERG	40	2.43	0.0150
	LERG	41	5.08	< 0.0001
Radio luminosity vs ICM luminosity, with a redshift correlation				
Matched	HERG	28	0.79	0.4296
z0.1 and ERA	LERG	27	4.69	< 0.0001
ICM luminosity vs temperature, with a redshift correlation				
z0.1	Spectrum	34	15.28	< 0.0001
z0.1 and ERA	Spectrum	44	18.35	< 0.0001
ICM luminosity vs B_{gq}, with a redshift correlation				
All	All	22	3.66	0.0002
Radio luminosity vs central density, with a redshift correlation				
z0.1	HERG	25	0.73	0.4654
	LERG	30	2.84	0.0046
ICM luminosity vs central density, with a redshift correlation				
	HERG	25	5.09	< 0.0001
	LERG	30	7.79	< 0.0001
Radio luminosity vs ICM luminosity, with a central density correlation				
	HERG	25	1.32	0.1868
	LERG	30	1.50	0.1336
Radio luminosity vs central density, with an ICM luminosity correlation				
	HERG	25	1.14	0.2542
	LERG	30	1.37	0.1706

N is sample size; τ is the partial correlation statistic; σ is the standard deviation; p is probability under the null hypothesis.
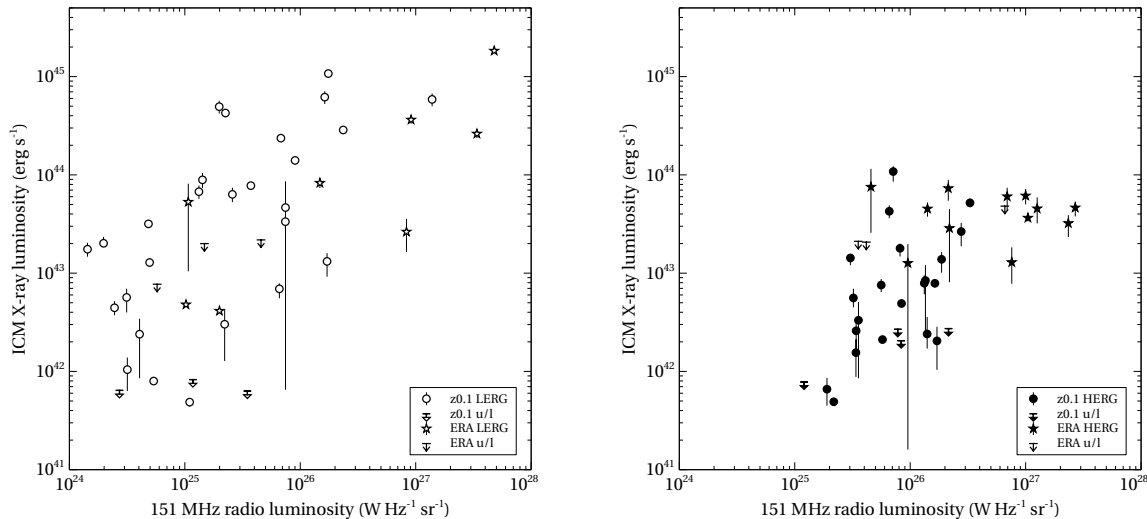
Figure 6. Radio luminosity vs ICM X-ray luminosity for the combined z0.1 and ERA samples, with LERGs on the left (empty symbols) and HERGs on the right (filled symbols). z0.1 sources are shown as circles and ERA sources as stars. z0.1 upper limits use triangles and ERA upper limits use arrows.

ronments at $z \sim 0.1$ than at $z \sim 0.5$. Is this effect genuine, or is it due to non-detection of weak environments at high redshift?

We would need observations of almost 1000 ks to measure ICM luminosities of 10^{42} erg s^{-1} at the redshifts of the ERA sample, so we cannot know whether the lack of high redshift sources in this region of the plot is real or due to insufficient observation time. We have a hint that there might be at least occasional objects in this region from Ramos Almeida et al. (2013) – they obtained an extremely low galaxy-quasar spatial covariance function (B_{gq}) for PKS1136−13, which has a radio luminosity of 2.7×10^{26} W Hz^{-1} sr^{-1}. If this source follows the expected correlation between L_X and B_{gq}, it would then lie well into the lower right portion of the $L_X - L_R$ plot. The 80 ks X-ray observation of this source shows no sign of ICM emission, but this observation is not long enough to detect emission below 10^{43} erg s^{-1}. However, this is the only 2Jy source in the high redshift range with such a low B_{gq} — the others have B_{gq} values that should place them in environments around and above 10^{43} erg s^{-1}. We also have only three upper limits in the ERA sample HERGs, and two of these are from short observations, so if there are weak environment sources at these redshifts then they are rare and are unlikely to have a dramatic affect on the sample medians. We therefore conclude that evolution of the HERG environment is probable but not certain.

5.1.4 Cluster morphology

The distributions of β and core radius are shown in Figure 2. The HERG and LERG sub-samples have slightly different β medians – 0.42 vs 0.52 – but a Wilcoxon-Mann-Whitney test shows no significant difference.

The median core radius for the full z0.1 sample is also different for the two sub-samples – 17 kpc for the HERGs and 62 kpc for the LERGs. In this case, the distributions of the HERGs and LERGs are different, and this is confirmed by the Wilcoxon-Mann-Whitney test (z=2.41, p=0.008), suggesting that the HERGs may have a higher concentration of gas near the cluster centre. However, when the core radius was scaled by R_{500} the difference is no longer very significant (z=1.79, p=0.037), so the difference in core

radius may be due to the difference in mass distributions between HERGs and LERGs rather than cluster shape.

5.1.5 Central density

If, as discussed in the Section 1, LERGs follow a cycle fuelled by gas from the ICM and controlled by the central entropy of the system, we would expect the jet power to be related to the central conditions. We would also expect that, since ICM luminosity is related to cluster mass, n_e should be related to the ICM luminosity. As discussed in Section 4.1, we used the electron density n_e at $0.1R_{500}$ as an indicator of the central conditions and compared it with radio luminosity.

Figure 9 shows the electron densities at $0.1R_{500}$ plotted against ICM luminosity and radio luminosity for the HERGs, and Figure 10 for the LERGs for the z0.1 sample (we did not include the ERA sample as at their redshift the angular size of $0.1R_{500}$ was too close to the PSF to obtain reliable densities). As expected, the central density correlates strongly with ICM luminosity for both types of radio galaxy. In addition, there appears to be a relationship between L_R and n_e for the LERGs, but not for the HERGs, and this is confirmed at the 99.5 per cent confidence level by the Generalised Kendall's Tau tests comparing L_X and L_R with n_e in the presence of a common dependence on redshift (Table 7).

This result could simply be a reflection of the $L_R - L_X$ relationships for the two galaxy types, but if jet power is related to central density for the LERGs, this would also contribute to the $L_R - L_X$ relation. We therefore looked for a correlation between L_R and L_X in the presence of a common dependence on n_e. If the jet power is in a large part controlled by central density, this should remove the correlation; if jet power and central density are unrelated then the correlation should be unchanged. As can be seen from Table 7, the partial correlation test of $L_R - L_X$ in the presence of n_e shows no significant correlation. However, performing the inverse test of looking for a correlation between L_R and n_e in the presence of a common dependence on L_X also removed the correlation, suggesting that all three factors were well correlated.

In an attempt to find which of the three possible relationships ($L_R - L_X$, $L_R - n_e$ and $L_X - n_e$) was dominant, we did a Princi-
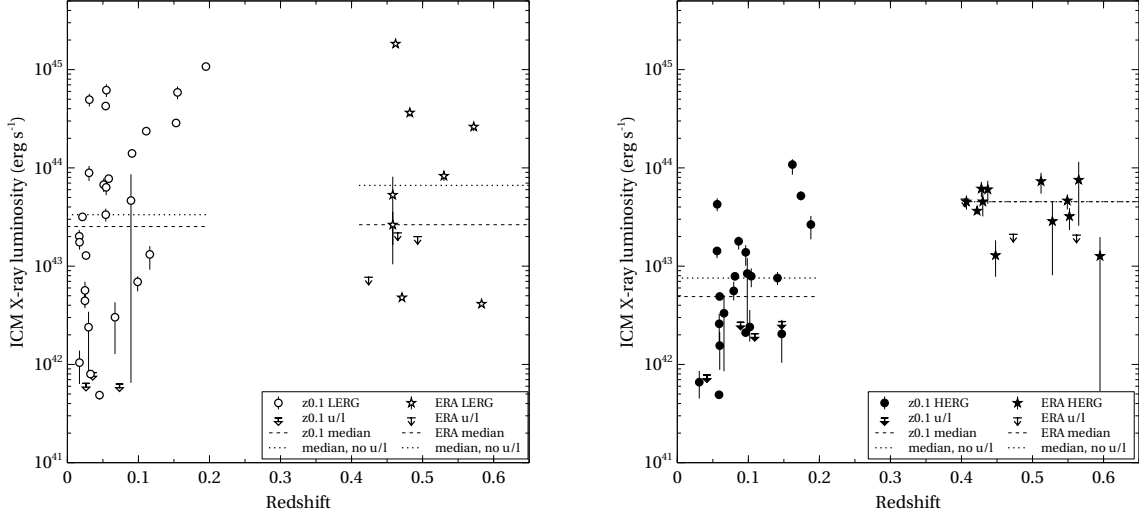
Figure 7. ICM X-ray luminosity vs redshift for the combined z0.1 and ERA samples, with LERGs on the left and HERGs on the right. Symbols as in Figure 6.
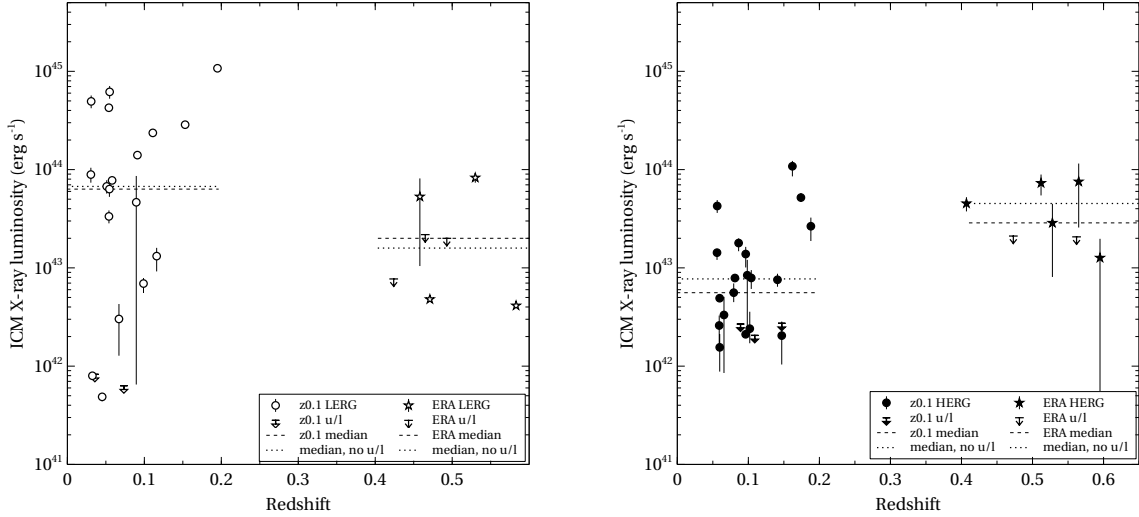
Figure 8. ICM X-ray luminosity vs redshift for sub-samples matched in radio luminosity of the z0.1 and ERA samples, with LERGs and HERGs on the right. Symbols as in Figure 6.

pal Components Analysis (PCA, Francis & Wills 1999) on the data with the upper limits excluded, having checked that this made little difference to the results of the Generalised Kendall's Tau tests. As can be seen from Table 9, the three factors all contribute in similar proportions to the main principal component PC1, suggesting that we cannot determine the dominant relationship from this data. This was confirmed using Spearman's ρ tests comparing the results of the full PCA with similar analyses on pairs of factors, which all gave similar and very strong correlations.

5.2   Comparison with general cluster and group environments

We assume in our analysis that the cluster environments of our radio-loud AGN do not differ markedly from those of clusters of similar luminosity without radio galaxies. We therefore compared our temperature-luminosity scaling relation with $L_X - T_X$ relations for other samples.

Table 9. Principal Component Analysis for radio luminosity, ICM luminosity and central density, using the $z0.1$ sample.

|	PC1	PC2	PC3
Eigenvalue	1.924	0.487	0.205
Proportion	0.736	0.186	0.078
Cumulative	0.736	0.922	1.000
Variable	PC1	PC2	PC3
Radio luminosity	0.495	0.646	0.581
ICM luminosity	0.646	0.296	0.407
Central density	0.581	-0.703	0.705

PC1, PC2 and PC3 are the principal components in order of contribution to the total variance.

There is a very strong correlation between ICM temperature and luminosity (Table 7). Figure 11 shows ICM temperature plotted against luminosity for all sources in the z0.1 and ERA samples with
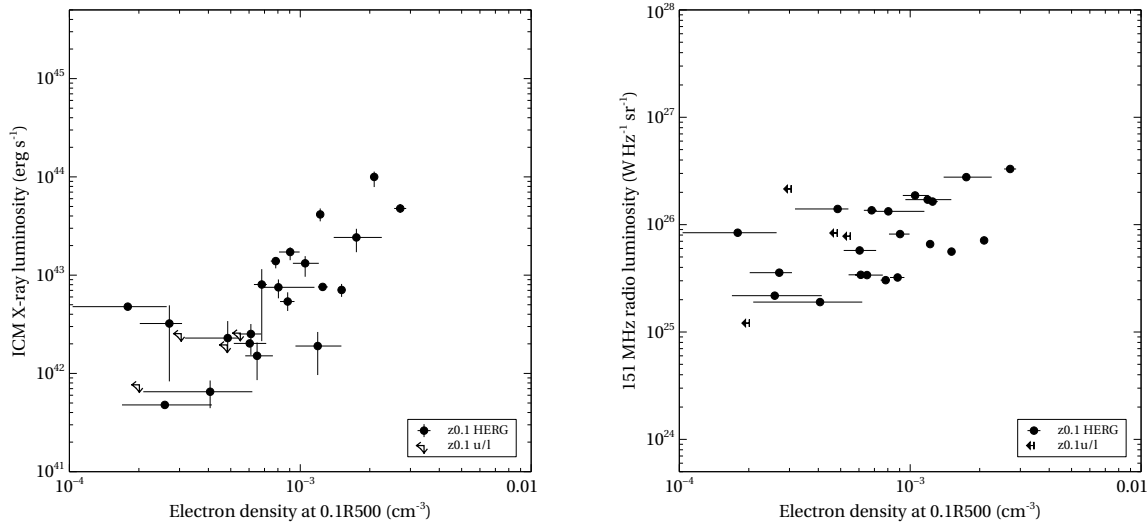
Figure 9. Density at $0.1R_500$ vs ICM X-ray luminosity(left) and radio luminosity (right) for HERGs in the z0.1 sample. Symbols as in Figure 6.
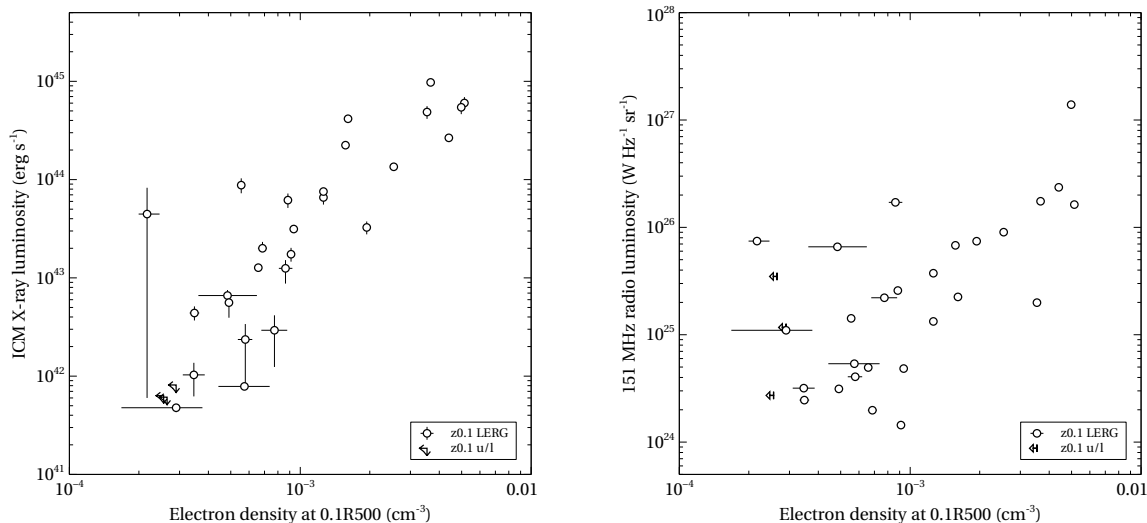
Figure 10. Density at $0.1R_500$ vs ICM X-ray luminosity(left) and radio luminosity (right) for LERGs in the z0.1 sample. Symbols as in Figure 6.

temperatures obtained by spectral analysis. We used the orthogonal BCES method from Akritas & Bershady (1996) to calculate the regression line (solid line, $log_{10}L_X = (3.56 \pm 0.36)log_{10}T_X + (42.40 \pm 0.15)$).

The dashed line shows the Pratt et al. (2009) $L_X - T_X$ scaling relation for the REXCESS clusters, which we used to obtain the estimated temperatures. Our slope is slightly higher (3.56 ± 0.36 vs 3.35 ± 0.32), but compatible. Also plotted in Figure 11 is the $L_X - T_X$ relation obtained be Stott et al. (2012) for clusters containing radio sources from the *XMM* Cluster Survey. Their slope of 2.91 ± 0.45 is lower than our result.

Our sample contains both galaxy groups and clusters, both cool-core and non-cool-core environments and consists entirely of radio galaxies. These factors have all been found to modify the $L_X - T_X$ relation (e.g. Helsdon & Ponman 2000; Croston et al. 2005; Chen et al. 2007; Magliocchetti & Brüggen 2007; Pratt et al. 2009; Ekmiller et al. 2011; Stott et al. 2012; Bharadwaj et al. 2015). In addition, selection biases (in particular the Malmquist bias, which ensures that for a given temperature, the most lumi-

nous objects are preferentially selected) can have a strong effect on the slope of the $L_X - T_X$ relation (e.g. Ekmiller et al. 2011; Bharadwaj et al. 2015), and the evolution parameter, which is usually assumed to be unity, is likely to be affected by the break in self-similarity in the $L_X - T_X$ relation (Maughan 2014).

Our relation is likely to be affected by all the factors mentioned above, but lies near or within most of the ranges cited by the literature and so our sample shows no evidence of being different from other cluster and group samples.

We also calculated entropy S within $0.1R_{200}$ for the sources from the z0.1 sample with temperatures obtained by spectral analysis. We used $h^{4/3}(z)S = kT/n_e^{2/3}$, where R_{200} is the radius at an overdensity of 200 (Arnaud et al. 2005), kT is the ICM temperature and n_e is the electron density. n_e was calculated as described in Section 4.1. The results are shown in Figure 12.

We obtained a regression line for the $S - T_X$ relation, again using the Akritas & Bershady (1996) orthogonal BCES method, and obtained a shallower slope than that of Pratt et al. (2010) (0.63 ± 0.13 vs 0.89 ± 0.15). Our slope does however lie within
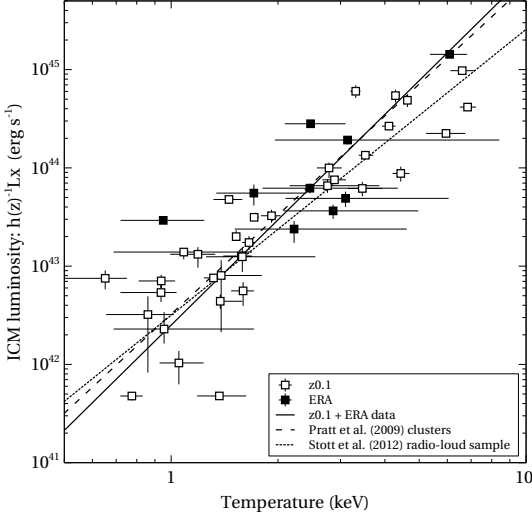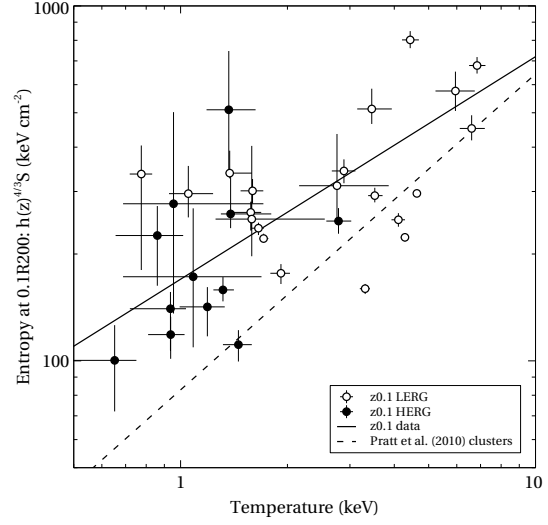
Figure 11. ICM luminosity vs temperature for the temperatures obtained by spectral analysis. Empty squares denote the z0.1 sample and filled squares the ERA sample. The solid line shows the $L_X - T_X$ relationship from the combined samples, and the dashed line shows Pratt et al. (2009)'s $L_X - T_X$ relation for clusters. Also shown is the relation from Stott et al. (2012) for their sub-sample of clusters containing radio galaxies (dotted line).

Figure 12. Entropy vs temperature for the z0.1 sample temperatures obtained by spectral analysis. Empty circles are LERGs and filled circles are HERGs. The solid line shows the $S - T_X$ relationship from the z0.1 sample and the dashed line shows Pratt et al. (2010)'s $S - T_X$ relation for clusters.

the range of results from the literature cited by Pratt et al. (2010) (slopes of 0.49 to 0.92). If, as discussed in Section 1, interactions form part of the triggering process for HERGs, we would expect them to have high entropy for their temperature. Pratt et al. (2010) noted that disturbed clusters tend to have high entropy compared with relaxed clusters of the same temperature, and indeed all but one of our HERG sample lie above their regression line.

Overall, there is no systematic evidence that the luminosities of our sample of radio galaxies differ from those of galaxy groups and clusters that do not host radio-loud AGN, so our use of luminosity as a proxy for total cluster mass is reasonable. Our entropies tend to be high, which is likely to be at least in part due to clusters being disturbed, but are still within the ranges cited in the literature.

Figure 13. ICM luminosity vs galaxy-quasar spatial covariance function B_{gq} for the 2Jy sources in the z0.1 sample. B_{gq} values were taken from Ramos Almeida et al. (2013). Empty circles are LERGs and filled circles are HERGs. The solid line shows the regression line for the data, and the dotted lines the 1σ scatter.

5.3   Comparison with optical measures

We would expect a correlation between different measures of cluster richness, though with a fair amount of scatter (e.g. Yee & Ellingson 2003; Ledlow et al. 2003, I13). Ramos Almeida et al. (2013) have calculated the galaxy-quasar spatial covariance function (B_{gq}) for the 2Jy sample. We therefore compared these with the ICM luminosities for the 2Jy sources within our z0.1 sample (Figure 13). A generalised partial τ showed a correlation at the 3σ level (Table 7). We used the Buckley-James method (Isobe et al. 1986) to obtain a regression line including the upper limits in L_X; this gave $log_{10}L_X = (0.0014 \pm 0.0003)B_{gq} + (42.58 \pm 0.59)$. The amount of scatter compromises the relationship's utility as a scaling relation, and the two measures were taken within different radii (170 kpc for B_{gq} and R_{500} (median 600 kpc) for L_X). However, the strength of the correlation shows that overall results from the two measures should be comparable.

5.4   Implications

Our results add evidence for a difference in cluster environments to the increasing wealth of data supporting a dichotomy in the population of radio-loud AGN, and provide supporting evidence for models that involve the different accretion cycles of the high and low excitation sources. This difference in cluster environments may also play a part in modifying radio galaxy polarisations, as suggested by O'Sullivan et al. (2015), who recently reported a dichotomy in the integrated degree of polarisation of HERGs and LERGs.

5.4.1 LERG results

The strong correlations between radio luminosity, ICM luminosity and central density for LERGs supports the concept of some form of relationship between ICM properties and jet power. This could provide corroborative evidence for a stable, long-lasting feedback cycle as demonstrated in the simulations of Gaspari et al. (2012, 2013), in which matter is driven outwards by the jets and falls inwards from the ICM when the central conditions become favourable. The pressure of available gas in the ICM will affect the flow of gas into the nucleus, which will in turn affect the accretion rate and the jet power. There will be some variation as the central regions heat up and then cool again as the gas clumps accrete and disperse and are recharged, and this may be one of the several factors that could contribute to the scatter in the $L_R - L_X$ plot. Other possible factors that might add scatter to the relationship are discussed briefly in I13 – the scatter in the relationship between mechanical jet power and total radio luminosity (e.g. Bîrzan et al. 2008; Cavagnolo et al. 2010; Godfrey & Shabala 2013; Hardcastle & Krause 2013) and the effect of differences in central gas properties (which are not correlated with ICM luminosity, e.g. Croston et al. 2008b) on jet power. It might be that the cyclic variations suggested by Gaspari et al. (2012, 2013) could contribute to both these issues.

An alternative explanation for the correlation is that it results at least in part from 'environmental boosting' (e.g. Barthel & Arnaud 1996; Hardcastle & Krause 2013), where for a given jet power, a richer environment increases the radio luminosity. However, this effect should apply equally to both HERGs and LERGs. The fact that the individual HERG samples show no correlation suggests that an explanation based on fuelling mechanism such as that described above is more likely. It also suggests that the environmental boosting may be counteracted by another mechanism. Entrainment is expected to increase with environment density and reduces radio luminosity relative to jet power (eg. Croston & Hardcastle 2014), and so works in the opposite direction to environmental boosting.

5.4.2 HERG results

Turning to the HERGs, the lack of correlation between the radio luminosity and cluster properties for the individual samples suggests that the ICM does not have a major rôle to play either in powering the system or in controlling the luminosity of the lobes. This fits in with the theory that HERGs accrete at a relatively high rate from an accretion disc maintained by a local reservoir of cold gas, probably originating from galaxy interactions and mergers (e.g. Hardcastle et al. 2007b; Ramos Almeida et al. 2012; Tadhunter et al. 2014). Gas ingestion from the ICM as described by Gaspari et al. (2013) is sufficient to fuel even the most powerful LERG jets, and is also sufficient to fuel low-power HERGs. It could not however maintain the accretion rates required to power the jets and nucleus of more powerful HERGs. The richness of the ICM would therefore be largely irrelevant and no correlation is to be expected.

If the difference between the HERG environments in the ERA and z0.1 environments does indicate evolution, then this is very interesting. At high redshifts ($z > 1$), radio galaxies are typically seen in richer environments than similar radio-quiet galaxies (Wylezalek et al. 2013; Hatch et al. 2014), but by $z \sim 0.5$ we are finding radio galaxies in groups and poor clusters. This may be due to cosmic downsizing — as the gas density in the vicinity of the black hole depletes as a result of AGN activity and star formation, then the conditions required for HERGs to be triggered, such as mergers bringing new gas into the host galaxy, occur in poorer environments as redshift reduces. However, although the minimum environment richness at $z \sim 0.1$ is lower than at $z \sim 0.5$ (as would be expected from cosmic downsizing) the maximum richness of the environments is the same. Thus there must be additional processes involved.

6 CONCLUSIONS

We have compared low frequency radio luminosity with the richness of the cluster environment for a sample of 55 radio-loud AGN lying in the redshift range $0.01 \leqslant z \leqslant 0.2$. The sample covered three decades of radio luminosity and contained 25 high excitation and 30 low excitation sources. We used the X-ray luminosity of the ICM as the measure of cluster richness. The X-ray observations were taken from the *Chandra* and *XMM-Newton* archives.

We found:

• For the complete z0.1 sample, a weak correlation between radio luminosity and cluster richness;

• For the LERG sub-sample, strong correlations between radio luminosity, cluster richness and central density;

• For the HERG sub-sample, no correlation between radio luminosity and cluster richness, or between radio luminosity and central density;

• The core radii of the LERGs were on average larger than those of the HERGs.

These results were similar to those of our previous study (I13), which used the ERA sample, containing 26 sources at higher redshift ($0.4 \leqslant z \leqslant 0.6$). We compared the results for $z \sim 0.1$ and $z \sim 0.5$, and found:

• For the two LERG samples, the slopes and normalisations of the radio luminosity–ICM richness correlation were very similar, giving a very strong correlation. This suggested that there had been no evolution with redshift since $z \sim 0.5$, and we found no significant difference between the cluster environments of the two samples;

• Although the HERGs in both samples had similar maximum environment richnesses, the lower redshift sample also included environments much weaker than any seen in the ERA sample, giving tentative evidence of evolution of the environment;

• The HERGs occupied groups and clusters with more compact central regions than the LERGs, suggesting that HERGs may have a greater concentration of gas near the host galaxy than LERGs;

• We found the luminosity-temperature relation for our samples to be compatible with $L_X - T_X$ relations derived for general samples of clusters and groups, suggesting that the environments occupied by radio-loud AGN are similar to those of typical clusters.

The evidence of a difference between the HERG and LERG large-scale environments is now strong, so we next intend to investigate relationships between the ICM and other factors where differences have been found between the two types of AGN.

The scientific results reported in this article are based on observations made with the *Chandra* X-ray observatory and on observations obtained with *XMM-Newton*, an ESA science mission with instruments and contributions directly funded by ESA Member States and NASA. This research has made use of software provided by the *Chandra* X-ray Center (CXC) in the application packages CIAO and CHIPS, and of the *XMM-Newton* Science Analysis Software (SAS). This research also made use of the University of Hertfordshire high-performance computing facility (http://stri-cluster.herts.ac.uk/). Figures were plotted using the *veusz* package (http://home.gna.org/veusz/).

REFERENCES

Akritas M.G., Bershady M.A., 1996, ApJ, 470, 706
Akritas M.G., Siebert J., 1996, MNRAS, 278, 919
Allen, M. G. et al., 2002, ApJS, 139, 411
Allen, S. W., Dunn R. J. H., Fabian A. C., Taylor G. B., Reynolds C. S., 2006, MNRAS, 372, 21
Arnaud M., Pointecouteau E., Pratt G.W., 2005, A&A, 441, 893
Balestra P. et al., 2007, A&A, 462, 429
Barthel P. D., Arnaud K. A., 1996, MNRAS, 283, L45
Baum S. A., Heckman T., Bridle A., van Breugel W., Miley G., 1988, ApJS, 68, 643
Belsole E., Worrall D.M., Hardcastle M.J., Croston J.H., 2007, MNRAS, 381, 1109
Best P.N., 2004, MNRAS, 351, 70
Best P.N., Heckman T.M., 2012, MNRAS, 421, 1569
Birkinshaw M., Worrall D.M. 1993, ApJ, 412, 568
Bharadwaj V., Reiprich T.H., Lovisari L., Eckmiller H.J., 2015, A&A, 573, A75
Bîrzan L., McNamara B.R., Nulsen P.E.J., Carilli C.L., Wise M.W., 2008, ApJ, 686, 859
Braito V., Reeves J. N., Sambruna R. M., Gofford J., 2011, MNRAS, 414, 2739
Bryant J. J., Hunstead R. W., 2002, MNRAS, 337, 861
Cavagnolo K.W. et al., 2010, ApJ, 720, 1066
Cavaliere A., Fusco-Femiano R., 1976, 49, 137
Chen Y., Reiprich T. H., Böhringer H., Ikebe Y., Zhang Y-Y., 2007, A&A, 466, 805
Chen R., Peng B., Strom R.G., Wei J., 2011a, MNRAS, 412, 2433
Chen R., Peng B., Strom R.G., Wei J., Zhao Y., 2011b, A&A, 529, A5
Chen R., Peng B., Strom R.G., Wei J., 2012, MNRAS, 422, 3004
Croston J. H., Hardcastle M. J., 2014, MNRAS, 438, 3310
Croston J. H., Hardcastle M. J., Birkinshaw M. 2005, MNRAS, 357, 279
Croston J. H., Hardcastle M. J., Birkinshaw M., Worrall D. M., Laing R. A. 2008a, MNRAS, 386, 1709
Croston J. H. et al., 2008b, A&A, 487, 431
Croston J. H. et al., 2011, ApJL, 734, L28
Croton D.J. et al., 2006, MNRAS, 365, 11
de Koff S. et al., 2000, ApJS, 129, 33
Dennett-Thorpe J., Scheuer P. A. G., Laing R. A., Bridle A. H., Pooley G. G., Reich, W., 2002, MNRAS, 330, 609
Dicken D., Tadhunter C., Morganti R., Buchanan C., Oosterloo T., Axon D., 2008, ApJ, 678, 712
Dickey J. M., Lockman F. J., 1990, ARA&A, 28, 215
Ekmiller H. J., Hudson D. S., Reiprich T. H., 2011, A&A, 535, A105

Evans D. A., Hardcastle M. J., Croston J. H., Worrall D. M., Birkinshaw M., 2005, MNRAS, 359, 363
Evans, D. A. et al. 2008, ApJ, 675, 1057
Feigelson E. D., Nelson P. I., 1985, ApJ, 293, 192
Fernandes C. A. C. et al., 2015, MNRAS, 447, 1184
Francis P. J., Wills B. J., 1999, in Fernland G., Baldwin J., eds, ASP Conf. Ser. Vol. 162, Quasars and Cosmology. Astron. Soc. Pac., San Francisco, p. 363
Frank, K. A., Peterson, J. R., Andersson, K., Fabian, A. C., Sanders, J. S., 2013, ApJ, 764, 46
Freyberg M.J., Pfeffermann E., Briel U.G., 2002, Proc. Symposium 'New visions of the X-ray universe in the XMM-Newton and Chandra era' 26–30 November 2001, ESTEC, The Netherlands, ESA SP-488
Fujita Y., Kawakatu N., Shlosman I., 2014, MNRAS, submitted
Gaspari M., Ruszkowski M., Sharma P., 2012, ApJ, 746, 94
Gaspari M., Ruszkowski M., Peng Oh S., 2013, MNRAS, 432, 3401
Gendre M. A., Best P. N., Wall J. V., Ker L. M., 2013, MNRAS, 437, 3071
Gizani N. A. B., Leahy J. P., 2003, MNRAS, 342, 399
Gizani N. A. B., Leahy J. P., 2004, MNRAS, 350, 865
Gliozzi M., Foschini L., Sambruna R. M., Tavecchio F., 2008, A&A, 478, 723
Godfrey L. E. H., Shabala S. S., 2013, ApJ, 767, 12
Grimberg B. I., Sadler E. M., Simkin, S. M., 1999, ApJ, 521, 121
Gürkan G., Hardcastle M. J., Jarvis M. J., 2014, MNRAS, 438, 1149
Gutierrez K., Krawczynski H., 2005, ApJ, 619, 161
Hardcastle M. J., 2004, A&A, 414, 927
Hardcastle M. J., Croston J. H., 2010, MNRAS, 404, 2018
Hardcastle M. J., Krause M. G. H., 2013, MNRAS, 430, 174
Hardcastle M. J., Croston J. H., Kraft R. P., 2007a, ApJ, 669, 893
Hardcastle M. J., Evans D. A., Croston J. H., 2007b, MNRAS, 376, 1849
Hardcastle M. J., Sakelliou I., Worrall D. M., 2005, MNRAS, 359, 1007
Hardcastle M. J. et al., 2007c, ApJ, 662, 166
Hardcastle M. J. et al., 2012, MNRAS, 424, 1774
Hardcastle M.J. et al., 2013, MNRAS, 429, 2407
Harvanek M., Ellingson E., Stocke J. T., 2001, AJ, 122, 2874
Hatch N. A. et al., 2014, MNRAS, 445, 280
Heckman T. M., Best P. N., 2014, ARA&A, 52, 589
Herbert P. D. et al. 2010, MNRAS, 106, 1841
Herbert P. D. et al. 2015, MNRAS, submitted
Helsdon S. F., Ponman T. J., 2000, MNRAS, 315, 356
Hodges-Kluck E. J., Reynolds C. S., Cheung C. C., Miller M. C., 2010, ApJ, 710, 1205
Hopkins P. F., Hernquist L., Cox T. J., Kereš D., 2008, ApJS, 175, 356
Ineson J., Croston J. H., Hardcastle M. J., Kraft R. P., Evans D. A., Jarvis M., 2013, ApJ, 770, 136
Inskip K. J. et al. 2010, MNRAS, 407, 1739
Ishibashi W., Fabian A. C., 2012, MNRAS, 427, 2998
Isobe T., Feigelson E. D., Nelson P. I., 1986, ApJ, 306, 490
Janssen R. M. J., Röttgering H. J. A., Best P. N., Brinchmann J., 2012, A&A, 541, A62
Joshi S. A., Nandi S., Saikia D. J., Ishwara-Chandra C. H., Konar C., 2011, MNRAS, 414, 1397
Kaastra J. S. et al., 1999, ApJ, 519, L119
Komossa, S., Bohringer, H., 1999, A&A, 344, 755

Kraft R. P., Azcona J., Forman W. R., Hardcastle M. J., Jones C., Murray S. S., 2006, ApJ, 639, 753

Kraft R.P. et al., 2007, ApJ, 659, 1008

Kraft R. P. et al., 2012, ApJ, 749, 19

Labiano A. et al., 2013, A&A, 549, 58

Laing R. A., Riley J. M., Longair M. S., 1983, MNRAS, 204, 151

Lanz L. et al., 2015, ApJ, 801, 17

Leahy J. P. et al., 1997, MNRAS, 291, 20

Ledlow M. J., Voges W., Owen F. N., Burns J. O., 2003, AJ, 126 2740

Lumb D. H., Warwick R. S., Page M., De Luca A., 2002, A&A, 389, 93

Magliocchetti M., Brüggen, M., 2007, MNRAS, 379, 260

Mahony E. K., Morganti R., Emonts B. H. C., Oosterloo T. A., Tadhunter, C., 2013, MNRAS, 435, L58

Mannering E., Worrall D. M., Birkinshaw M., 2013, MNRAS, 431, 858

Markevitch M. et al., 2003, ApJ 583, 70

Martizzi D., Jimmy, Teyssier R., Moore B., 2014, MNRAS, 443, 1500

Maughan B. J., 2014, MNRAS, 437, 1171

McLure R. J., Dunlop J. S., 2001, MNRAS, 321, 515

McNamara B. R., Nulsen, P. E. N., 2012, New J. Phys., 14, 055023

Miller N. A., Owen F. N., Burns J. O., Ledlow M. J., Voges W., 1999, AJ, 118, 1988

Mingo B. et al., 2014, MNRAS, 440, 269

Morganti R., Killeen N. E. B., Tadhunter C. N., 1993, MNRAS, 263, 1023

Morganti R., Oosterloo T., Tadhunter C. N., Aiudi R., Jones P., Villar-Martin M., 1999, A&AS, 140, 335

Mulchaey J., 2000, ARA&A, 38, 289

Narayan, R., Yi, I., 1994, ApJ, 428, L13

Nesvadba N. P. H., Boulanger F., Lehnert M. D., Guillard P., Salome P., 2011, A&A, 536, L5

Nulsen P. E. J. et al., 2005, ApJL, 625, 9

Nulsen P. E. J. et al., 2013, ApJ, 775, 117

O'Dea C. P., Baum S. A., Tremblay G. R., Kharb P, Cotton W., Perley R., 2013, ApJ, 771, 38

Okuda T., Kohno K., Iguchi S., Nakanishi K., 2005, ApJ, 620, 673

O'Sullivan S. P., Gaensler B. M., Lara-López M. A., van Velzen S., Banfield J. K., Farnes, J.S., 2015, ApJ, 806, 830

Pizzolato F., Soker N., 2005, ApJ, 632, 821

Pratt G. W., Croston J. H., Arnaud M., Böhringer H., 2009, A&A, 498, 361

Pratt G. W. et al., 2010, A&A, 511, 85

Prieto M.A., Zhao H., 1997, MNRAS, 290, 34

Ramos Almeida, C. et al., 2011, MNRAS, 410, 1550

Ramos Almeida C. et al., 2012, MNRAS, 419, 687

Ramos Almeida C. et al., 2013, MNRAS, 436, 997

Rinn A. S., Sambruna R. M., Gliozzi M., 2005, ApJ, 621, 167

Russell H. R., McNamara B. R., Edge A. C., Hogan M. T., Main R. A., Vantyghem A. N., 2013, MNRAS, 432, 530

Sadun A. C. Morrison P., 2002, AJ, 123, 2312

Schaye J. et al., 2015, MNRAS, 446, 521

Schellenberger G., Reiprich T. H., Lovisari L., Nevalainen J., David L., 2015, A&A, 575, 30

Shakura N. I., Sunyaev R. A., 1973, A&A, 24, 337

Shelton, D. L., 2011, MSc Thesis, University of Hertfordshire

Sijacki, D., Springel, V., 2006, MNRAS, 366, 397

Simionescu A. et al., 2009, A&A, 495, 721

Simpson C., Ward M., Clements D. L., Rawlings S., 1996, MN-RAS, 281, 509

Smolčić V., 2009, ApJ, 669, L43

Son D. et al., 2012, ApJ, 757, 140

Stott J. P. et al., 2012, MNRAS, 422, 2213

Strom R., Chen R., Yang J., Peng B., 2013, MNRAS, 430, 2090

Tadhunter C. N., Morganti R., di Serego-Alighieri S., Fosbury R. A. E., Danziger I. J., 1993, MNRAS 263, 999

Tadhunter C. N. et al., 2014, MNRAS, 445, L51

Tasse C., Best P. N., Röttgering H., Le Borgne D., 2008, A&A, 490, 893

Tombesi F., et al., 2010, ApJ, 719, 700

Tremblay G. R., et al., 2006, ApJ, 643, 101

Tremblay G. R., et al., 2010, ApJ, 715, 172

van der Wolk G., Barthel P. D., Peletier R. F., Pel J. W., 2010, A&A, 511, A64

Voit G. M., Donahue M., 2015, ApJ, 799L, 1

Wall J. V., Peacock J. A., 1985, MNRAS, 216, 173

Weil K, Roberts D. H., 2014, American Astronomical Society, AAS Meeting 224, 221.16

Wills K. A., Morganti R, Tadhunter C. N., Robinson T. G., Villar-Martin M., 2004, MNRAS, 347, 771

Worrall D. M., Birkinshaw M., Kraft R. P., Hardcastle M. J., 2007, ApJ, 658, L79

Wold M., Lacy M., Lilje P. B., Serjeant S., 2000, MNRAS, 316, 267

Wylezalek D. et al, 2013, ApJ, 769, 79

Yee H. K. C., Ellingson E., ApJ, 2003, 585, 215

APPENDIX A: NOTES ON INDIVIDUAL SOURCES

A1 3CRR sources

3C 28 (A115-N, PKS 0053+26) is a LERG with FRII morphology. Its host is one of a pair of merging clusters and is highly asymmetric, and the disturbance is visible in the surface brightness profile. Both clusters are rich – Gutierrez & Krawczynski (2005) obtained values of around 5 keV for the individual clusters away from the merger and 8 keV for the plasma between the clusters. Because we are interested in the full environment around the host galaxy, we included parts of both regions and obtained a temperature of $6.61^{+0.59}_{-0.49}$ keV. This lies within the upper bound of the temperature of $5.35^{+1.28}_{-0.09}$ keV obtained by Shelton (2011).

Our luminosity lies very close to the value expected from the $L_X - T_X$ relation. It is higher than that obtained by Shelton (2011) — our surface brightness profile is substantially wider, perhaps because of our use of double background subtraction and double β modelling.

3C 31 (NGC 383) is a LERG with a massive central rotating disc of molecular gas (Okuda et al. 2005) and FRI morphology. Our temperature of 1.53 ± 0.3 keV is consistent with the those obtained by Komossa & Bohringer (1999) and Croston & Hardcastle (2014). Hodges-Kluck et al. (2010) found a higher temperature ($2.0^{+0.5}_{-0.02}$ keV) in the central regions with a *Chandra* observation.

3C 33 (PKS 0106+13) is a Narrow Line Radio Galaxy (NLRG) with FRII morphology lying in a weak environment. The radio outburst is thought to be energetic enough to eject a significant fraction of the corona gas (Kraft et al. 2007). We detected very little emission beyond the host galaxy. The counts are low so we

obtained an estimated temperature (1.1 keV). This is typical of a group environment.

3C 35 is also an NLRG with FRII radio structure in a weak environment. Mannering et al. (2013) report a gas 'belt' lying around the source between the lobes and extending out to about 170 kpc – not far short of our detected radius of emission. We found a broad surface brightness profile and an estimated temperature of 1 keV, very similar to the spectral temperature obtained by Mannering et al. (2013) using combined *Chandra* and *XMM-Newton* observations.

3C 66B is a LERG with FRI morphology. Our temperature of 1.7 keV is compatible with that of Croston et al. (2008a), but we obtained a higher luminosity ($3.17^{+0.10}_{-0.12}$ vs $1.07^{+0.08}_{-0.24} \times 10^{43}$ erg s^{-1}). The reason for the discrepancy is not clear, but could relate to the use of an improved background subtraction method in this work.

3C 76.1 is a LERG with FRI plumes spreading across a large proportion of the detected environment, which we found to be weak. Miller et al. (1999), using the *ROSAT* All-Sky Survey, did not detect any extended emission. Because of the low counts (this was a short observation), we could not fit a double-β model. We used an estimated temperature of 0.65 keV. This is lower than the $0.91^{+0.25}_{-0.14}$ keV obtained by Croston et al. (2008a) with an *XMM-Newton* observation; our luminosities are however compatible.

3C 98 (PKS 0356+10) is an NLRG with FRII morphology in a weak environment with the detected emission not extending far beyond the host galaxy. Again, Miller et al. (1999) did not detect extended emission. We used an estimated temperature of 0.62 keV. This was lower than the $1.1^{+0.3}_{-0.2}$ keV obtained by Hodges-Kluck et al. (2010) within a smaller radius.

3C 192 (PKS 0802+24) is another NLRG with FRII morphology in a weak environment. This was a short observation, and although the emission extended beyond the host galaxy, there were insufficient counts to fit a double-β model. We used an estimated temperature (0.8 keV).

3C 219 is a Broad Line Radio Galaxy (BLRG) with FRII morphology. It may be recently re-triggered after a dormant period (Weil & Roberts 2014) as it has a small jet within a well-formed pair of lobes with a classical double structure.

The temperature (1.5 keV) and luminosity (5.2×10^{43} erg s^{-1}) are those of a group, and are compatible with those obtained by Shelton (2011).

3C 236 is a LERG with massive FRII lobes extending well beyond the imaging chips. It is a double-double, with outer lobes of 4 Mpc in extent and inner lobes of 2 kpc (Tremblay et al. 2010). It is thought to have been reactivated about 10^5 years ago (Labiano et al. 2013). We found a weak environment, with insufficient counts for spectral analysis. Our estimated temperature of 1.2 keV is that of a group environment.

3C 285 is an NLRG with FRII morphology in a highly disturbed group environment. The host galaxy is also highly disturbed, probably as a result of a recent merger (Allen et al. 2002), and is currently interacting with another galaxy (Baum et al. 1998). We obtained a temperature of $0.94^{+0.10}_{-0.22}$ keV for the extended emission, consis-

tent with Hodges-Kluck et al. (2010). Hardcastle et al. (2007c) obtained a lower temperature of 0.64 keV with a MEKAL model; we found compatible results when we replaced our APEC model with a MEKAL model.

Our surface brightness profile, generated with a double β model and double background subtraction, gave a wider profile than that obtained by Hardcastle et al. (2007c), and our luminosity is consequently higher – $0.56^{+0.14}_{-0.11}$ vs $0.19^{+0.1}_{-0.1} \times 10^{43}$ erg s^{-1}.

3C 293 is a LERG with FRI plumes in a weak environment. It is a double-double source with estimated ages of ~ 20 Myr for the outer lobes and $\lesssim 0.1$ Myr for the central source (Joshi et al. 2011), and has strong, jet-driven outflows of gas (Mahony et al. 2013; Lanz et al. 2015). We obtained a temperature of 0.78 keV – a weak group temperature. We found the emission to be under-luminous for its temperature.

3C 296 (NGC 5532, PKS 1414+11) is a LERG with FRI morphology and occupies a group environment – Miller et al. (1999) found 4 galaxies in the group. The source is relatively near and the emission extends to just beyond the imaging chip. We therefore could not use double subtraction for modelling the profile, but were able to use one of the outer chips to model the background and so used double subtraction for the spectral analysis.

Croston et al. (2008a), using an *XMM-Newton* observation, obtained a temperature of 0.9 keV over a 50-600 arcsec region (larger than was available with our *Chandra* observation), but found that the temperature was higher (~ 1.4 keV), albeit with large errors, towards the centre. We also found that the temperature dropped gradually beyond around 150 arcsec, and so used the temperature within this region (1.6 keV). Hodges-Kluck et al. (2010) found the temperature to be 4 keV within a similar region, which is high compared with the results of Croston et al. (2008a) and our current work.

3C 303 is a BLRG with FRII structure at a steep angle to the viewer, and we found emission typical of a group environment. The observation had some pile-up, so we excluded the central 1.5 arcsec in the surface brightness profile. Our temperature and luminosity are slightly lower than those obtained by Shelton (2011) – $0.94^{+0.09}_{-0.13}$ vs $1.86^{+3.00}_{-0.54}$ keV and $0.76^{+0.12}_{-0.11}$ vs $0.92 \pm 0.06 \times 10^{43}$ erg s^{-1}. Our luminosity is a little high compared with the $L_X - T_X$ relation, but within the scatter.

3C 305 is a NLRG with a halo around the host galaxy, probably of material being driven out by the jets (Hardcastle et al. 2012). It has unusual FRII lobes spreading at right-angles to the jets. In common with Hardcastle et al. (2012) and Miller et al. (1999), we found little evidence of ICM emission beyond the host galaxy, and so we derived upper limits for this source.

3C 310 (PKS 1502+26) is a LERG with wide FRI plumes and a disturbed environment containing a large cavity, filamentary structure and a shock front at about 180 kpc from the nucleus (Kraft et al. 2012). The emission extends beyond the observing chip, but we were able to use one of the outer chips to model the background for the spectral analysis. We obtained a temperature of 1.9 keV, typical of a strong group or weak cluster.

3C 321 (PKS 1529+24) is an NLRG with FRII morphology in the process of merging with a neighbouring galaxy (Evans et al. 2008). The environment is weak and highly disturbed; we found

little emission beyond the host galaxy and had low counts, so we used an estimated temperature of 0.87 keV.

3C 326 (PKS 1550+20) is a LERG with large FRII lobes extending beyond the imaging chip. It shows evidence of molecular reservoirs thought to be formed by positive feedback (Nesvadba et al. 2011). The host galaxy has a nearby companion. We found the environment to be wide and flat and fairly weak. We had insufficient counts for spectral analysis so used an estimated temperature of 1.9 keV.

3C 338 (NGC 6166) is a LERG with FRI morphology, lying in the cluster Abell 2199. The cluster is highly disturbed, and Nulsen et al. (2013) discuss a variety of features in the cluster plasma including a shock front at 100 arcsec and a large plume extending to about 50 arcsec probably resulting from a cluster merger. These are visible in our surface brightness profile.

Our emission extends well beyond the imaging chip so double subtraction was not possible for either the profile or the spectral analysis. Nulsen et al. (2013) give a detailed temperature map of the centre of the cluster showing complex structure, and we obtained temperatures rising from a cooler centre in line with their results. Our overall temperature of 4.63 ± 0.08 keV is consistent with those reported by Kaastra et al. (1999) (using a *ROSAT* observation) and Hodges-Kluck et al. (2010).

3C 346 (4C 17.70, PKS 1641+17) is an NLRG with FRI morphology lying in a weak cluster. Our temperature of 2.8 keV is consistent with that of Shelton (2011). Our profile shows the same features as that of Shelton (2011), but has a much larger detected radius and a shallower outer slope, perhaps due to improved background modelling from the double subtraction. Our luminosity is therefore substantially higher (10.8 vs 0.65×10^{43} erg s^{-1}) and lies close to the $L_X - T_X$ relationship.

3C 386 (PKS 1836+17) is a LERG with broad $H\alpha$ lines in the spectrum (Simpson et al. 1996) and FRI lobes. The observation had low counts after background subtraction so we were unable to fit a double-β profile. There were insufficient counts left after subtraction of the *Chandra* blank sky files to obtain a background for the spectral analysis so we used single subtraction using a background from the observing chip to obtain the temperature, which was that of a group (1 keV).

3C 388 is a LERG in a cluster with cavities around its FRII lobes and a sub-cluster to the east (Kraft et al. 2006). The emission extends beyond the imaging chips, but we were able to use a side chip to model the background. We found a cluster temperature of 3.5 keV.

Our temperature and metallicity for the extended ICM agree with the results of Kraft et al., but our temperature is slightly higher than that obtained by Hodges-Kluck et al. (2010); this is probably due their use of a different (frozen) metallicity.

3C390.3. This BLRG has fast gas outflows from the central regions (Tombesi et al. 2010). It has FRII morphology and is in a strong environment. The ICM emission extends beyond the imaging chip, and the observation also suffers from considerable pileup. The temperature we obtained using single subtraction with the *Chandra* blank sky files was low for such bright emission (<1 keV). We had very few counts left after the *Chandra* blank sky subtraction and could not analyse a background spectrum, so it is possible that the

blank sky files were not accurate for this region or that the effects of the pileup extended across a wide energy range. We therefore used an estimated temperature for this source.

3C 433 (4C 24.54, PKS 2121+24) is an NLRG with hybrid FRI/FRII morphology in a group environment. The northern lobe is very bent, perhaps due to interaction with the surrounding ICM (Hodges-Kluck et al. 2010). We obtained a temperature consistent with that of Hodges-Kluck et al. (2010), but slightly lower than that of Shelton (2011). Our luminosity is higher than that of Shelton (2011) – $0.24^{+0.12}_{-0.07}$ vs $0.05 \pm 0.01 \times 10^{43}$ erg s^{-1} – but lies on the $L_X - T_X$ relationship. As with 3C 28, our modelling methods resulted in a much wider profile than that obtained by Shelton (2011).

3C442A (PKS 2212+13) is a LERG with FRI plumes, hosted by the interacting galaxy pair NGC 7236/7237 (Worrall et al. 2007), with filaments from the interacting galaxies and a ridge structure between the plumes (Hardcastle et al. 2007c). Worrall et al. (2007) found no evidence of an active jet, and suggest that the jets may have been stopped by an excess of central gas pressure resulting from the merger. The system lies in a weak cluster, and extends beyond the imaging chip. We could not obtain a background from the outer chips so used the *Chandra* blank sky files for the background for the spectral analysis. We obtained a temperature consistent with that of Hardcastle et al. (2007c), and a luminosity close to the $L_X - T_X$ relation.

3C 449 is a LERG with FRI plumes extending well beyond the imaging chip, and is relatively close, so the environment emission extends beyond the chip. It has a 600 pc dust disk which, unusually, lies nearly parallel to the jet (Tremblay et al. 2006). The surface brightness profile is wide with an unusually shallow slope, though well constrained by the MCMC modelling.

Our temperature of $1.66^{+0.06}_{-0.07}$ keV is higher than that obtained from a *XMM-Newton* observation by Croston et al. (2008a) (0.98 ± 0.02 keV), but was measured over a smaller region. Hodges-Kluck et al. (2010) obtained a temperature of 1.58 ± 0.06 keV over a smaller region still; their modelling included the contribution of the host galaxy, which we excluded.

Our luminosity of $1.75^{+0.28}_{-0.28} \times 10^{43}$ erg s^{-1} is slightly higher than that obtained by Croston et al. (2008a) ($1.20^{+0.12}_{-0.10} \times 10^{43}$ erg s^{-1}), but because of our higher temperature, our luminosity is calculated within a larger radius.

3C 452 is an NLRG with FRII morphology. There is a lot of X-ray emission associated with the radio structure, but beyond this the environment is poor. Having excluded the emission associated with the lobes, Shelton (2011) found a temperature of 1.18 ± 0.11 keV in the inner 160 arcsec, and $0.86^{+0.13}_{-0.05}$ keV beyond. We also found that the temperature dropped as the radius increased, but had a slightly higher temperature of $1.32^{+0.10}_{-0.08}$ keV in the central region.

3C 465 is a LERG with large, bent FRI plumes lying in a cluster. The cluster has a cool core with the temperature increasing to around 5 keV before levelling off (Hardcastle et al. 2005). We obtained an overall temperature of $4.43^{+0.26}_{-0.23}$ keV, consistent with the results of Hardcastle et al. (2005) and Hodges-Kluck et al. (2010).

4C73.08 is an NLRG with FRII morphology lying in a weak environment with unusual radio features (Strom et al. 2013). We did not detect much emission beyond the host galaxy and

could only fit a single-β model. Chen et al. (2012) identified 9 group members. Our temperature of 1.4 keV seems a little high for the weak environment, and we found the ICM under-luminous for the temperature compared with the $L_X - T_X$ relation.

DA 240 is a LERG with large FRII lobes. Although it lies in a respectable group of more than 30 galaxies (Chen et al. 2011a), Miller et al. (1999) failed to detect any X-ray emission from the ICM with a *ROSAT* observation. We likewise detected no emission beyond the host galaxy, and so obtained upper limits on the temperature and luminosity.

NGC 6109 (4C 35.40) is a LERG with a long narrow-angle-tail plume lying in a group of 13 galaxies (Miller et al. 1999). We found a weak environment beyond the host galaxy, but had insufficient counts to obtain a spectrum. We obtained an estimated temperature of 0.9 keV.

NGC 6251. This LERG has large FRI plumes extending beyond the imaging chip. It lies in a group of at least 20 galaxies (Chen et al. 2011b), and we detected emission extending beyond the chip. We could not model the background on the outer chips, so obtained the temperature using the single subtraction method with the *Chandra* blank sky files. We obtained a range of temperatures ranging from ~ 1 to ~ 2.5 keV from different regions, and used an intermediate result of $1.38^{+0.21}_{-0.03}$ keV, compatible with that found by Evans et al. (2005) using *XMM-Newton* observations.

We found a much higher luminosity than Evans et al. (2005) (0.44 ± 0.07 vs $0.07 \pm 0.01 \times 10^{43}$ erg.s^{-1}), but a slightly lower luminosity than that which Chen et al. (2011b) estimated from the galaxy velocity dispersions ($\sim 0.57 \times 10^{43}$ erg.s^{-1}. Our surface brightness profile was wider than that of Evans et al. (2005) and had a shallower β. This may be because our *Chandra* observation had a much smaller PSF than the *XMM-Newton* observation used by Evans et al. (2005), allowing a more detailed modelling of the surface brightness profile, or because the *Chandra* blank sky files underestimated the background emission. Our result is however close to the $L_X - T_X$ relation.

NGC 7385 (4C 11.71) is a LERG with small FRI plumes. Miller et al. (1999) found a weak extended environment with a group of 17 galaxies; we found very few counts beyond the host galaxy emission and so obtained upper limits for the temperature and luminosity.

A2   2Jy sources

PKS 0034−01 (3C 15) is a LERG with small FRII lobes in a weak environment ($B_{gq} \sim 90$ – Ramos Almeida et al. 2013). Like Rinn et al. (2005), we found insufficient evidence of ICM emission for analysis so we calculated upper limits for the temperature and luminosity.

PKS 0038+09 (3C 18) is a BLRG with small FRII lobes in a weak environment ($B_{gq} \sim 35$ – Ramos Almeida et al. 2013). The short observation time gave us insufficient counts for spectral analysis, so we used an estimated temperature of 1.8 keV.

PKS 0043−42. This is a spectroscopic LERG with FRII morphology lying in a weak cluster ($B_{gq} \sim 250$ – Ramos Almeida et al. 2013) and with evidence of a dusty torus (Ramos Almeida et al. 2011). The host galaxy was small in angular extent so we could

not model it separately. We found a temperature typical of a group/weak cluster (1.6 keV).

PKS 0213−13 (3C 62) is an NLRG with small FRII lobes in a weak environment ($B_{gq} \sim 60$ – Ramos Almeida et al. 2013). We detected little emission beyond the host galaxy, and had insufficient counts for a double-β model or for spectral analysis. Our estimated temperature of 0.85 keV is typical of a weak group.

PKS 0349−27 is an NLRG with FRII morphology and extended regions of ionised gas (Grimberg et al. 1999), perhaps resulting from a previous merger. We found a temperature typical of a weak group environment (0.86 keV); Ramos Almeida et al. (2013) found a stronger B_{gq} than we would expect for that temperature ($B_{gq} \sim 200$).

PKS 0404+03 (3C 105) is an NLRG with FRII morphology. Ramos Almeida et al. (2013) found that it lay in a weak environment ($B_{gq} \sim 80$). The observation time is short, and we found only very slight evidence of ICM emission beyond the host galaxy. We therefore derived upper limits for this source.

PKS 0442−28. This is also an NLRG with FRII morphology. We found no evidence of ICM emission beyond the host galaxy, so derived upper limits for this source. There are however several galaxies close to the host, and Ramos Almeida et al. (2013) found a B_{gq} of ~ 450.

PKS 0620−52 is a LERG with FRI plumes lying at a steep angle to each other. It lies in a cluster ($B_{gq} \sim 900$ – Ramos Almeida et al. 2013). The emission extended beyond the imaging chips, and we were also unable to use a side chip to model the background. We used the *Chandra* blank sky files for the background for both the profile and the spectral analysis. Our temperature of 2.8 keV is typical of a weak cluster.

PKS 0625−35. This source has an optical classification of LERG, but is classified by Wills et al. (2004) as a possible BL Lac object and by Gliozzi et al. (2008) as a LERG. It has FRI morphology and lies in cluster A 3392 ($B_{gq} \sim 5000$ – Ramos Almeida et al. 2013). We obtained a cluster temperature (3.5 keV). The emission extended beyond the imaging chip so we used the *Chandra* blank sky files for the background for both the profile and the spectral analysis.

PKS 0625−53 is a LERG with a FRII morphology lying in a disturbed cluster (A 3391). The emission extended beyond the imaging chip but we were able to use the spectrum from one of the side chips to model the background. We obtained a higher temperature than Frank et al. (2013) ($6.84^{+0.38}_{-0.34}$ vs 5.21 ± 0.03 keV). This difference is in line with that expected from the reported difference between temperatures obtained using *Chandra* and *XMM-Newton* (Schellenberger et al. 2015).

This is our hottest ICM, although not the most luminous, and it lies slightly below the $L_X - T_X$ relation – the *XMM-Newton* temperature of Frank et al. (2013) would bring the source onto the $L_X - T_X$ relation.

PKS 0806−10 (3C 195). The host galaxy of PKS 0806−10 may be interacting with a nearby galaxy (Inskip et al. 2010). It is an NLRG with FRII morphology. Although Ramos Almeida et al. (2013) found a strong group/weak cluster environment ($B_{gq} \sim 600$), we

found little emission beyond the host galaxy so used an upper limit.

PKS 0915−11 (Hyd A, 3C 218) is a LERG with FRI morphology lying in cluster Abell 780 ($B_{gq} \sim 800$ – Ramos Almeida et al. 2013). There is a large shock at about 300 arcsec (Simionescu et al. 2009). The emission extended beyond the imaging chips, and we were also unable to use a side chip to model the background so we used the *Chandra* blank sky files for the background for both the profile and the spectral analysis.

We obtained a temperature profile of a very similar shape to that reported by Simionescu et al. (2009) using an *XMM-Newton* observation, but with a higher temperature in line with the *Chandra* and *XMM-Newton* difference reported by Schellenberger et al. (2015). Hardcastle & Croston (2010) obtained a slightly higher temperature for a region nearer the nucleus, but it is compatible with our values for the temperature profile in that region.

PKS 0945+07 (3C 227). There is a dust torus around this BLRG extending to $\sim$ 0.5 kpc (van der Wolk et al. 2010) and an emission line region extending to $\sim$ 100 kpc (Prieto & Zhao 1997). It is an FRII lying in a weak environment ($B_{gq} \sim 80$ – Ramos Almeida et al. 2013). The detected emission does not extend far beyond the host galaxy, so we had insufficient counts for spectral analysis. Our estimated temperature of 1.6 keV is that of a group environment.

PKS 1559+02 (3C 327) is an NLRG with a possible double nucleus and dust lanes (de Koff et al. 2000; Ramos Almeida et al. 2011). It has FRII radio morphology. Ramos Almeida et al. (2013) found a strong group environment ($B_{gq} \sim 500$), but we found the ICM emission to be weak with a temperature of only 0.65 keV. The surface brightness profile is very wide and shallow, and we fixed the β parameter at the lower limit. Perhaps because of this, we found the luminosity to be high for the temperature compared with that expected from the $L_X - T_X$ relation.

PKS 1648+05 (Her A, 3C 348) is a LERG with radio characteristics of both FRI and FRII morphologies (Sadun & Morrison 2002). It has a strong, disturbed environment, a secondary nucleus with a strong shock front (Nulsen et al. 2005), and entrained gas and dust filaments that may have come from a now stripped companion galaxy (O'Dea et al. 2013). The shock front is clearly visible in the surface brightness profile.

The emission extended beyond the imaging chip but we were able to use the spectrum from the outer regions to model the background. Our temperature of 4.34 ± 0.11 keV is that of a moderate cluster, and is consistent with those reported by Nulsen et al. (2005) and Gizani & Leahy (2004) for the unshocked gas (using a shorter *Chandra* observation and a *ROSAT* observation respectively). Hardcastle & Croston (2010) obtained a slightly higher temperature from a smaller region nearer the nucleus and crossing the shock front; their temperature was compatible with a similar region in our temperature profile. Ramos Almeida et al. (2013) found that PKS 1648+05 is in a strong group ($B_{gq} \sim 500$) — a weaker environment than expected from our temperature.

Gizani & Leahy (2004) obtained a bolometric luminosity of 4.84×10^{44} erg s^{-1} within a radius of 500 kpc; we obtained a luminosity of 5.9×10^{44} erg s^{-1} within 938 kpc.

PKS 1733−56. This source is a BLRG with FRII morphology lying in a disturbed environment and accreting gas from a merging galaxy (Bryant & Hunstead 2002). We found an unusually wide

profile, perhaps a result of the disturbance, with a temperature typical of a group (1.4 keV). Ramos Almeida et al. (2013), however, found a very weak environment ($B_{gq} \sim 10$).

PKS 1839−48 is a LERG with a double nucleus (Ramos Almeida et al. 2011). It has FRI plumes and lies in a rich environment. Ramos Almeida et al. (2013) found a B_{gq} of around $\sim$ 1600, and we obtained a correspondingly high ICM temperature (6 keV).

PKS 1949+02 (3C 403) is an NLRG with X-shaped, FRII morphology lying in a weak environment. We replicated the ISM temperature of 0.24 keV found by Hodges-Kluck et al. (2010), but had insufficient counts for spectral analysis of the extended emission. We therefore used an estimated temperature of $0.93^{+0.07}_{-0.12}$ keV. This is a little hotter than the ICM temperature of 0.6 ± 0.2 obtained by Hodges-Kluck et al. (2010). Ramos Almeida et al. (2013) obtained a group-type environment ($B_{gq} \sim 120 - 300$).

PKS 1954−55. This is a LERG with FRI morphology lying in a rich group environment ($B_{gq} \sim 500$ – Ramos Almeida et al. 2013). The emission extended beyond the imaging chips, but we were able to use a side chip to model the background for the spectral analysis. Our temperature is that of a weak cluster (2.9 keV).

PKS 2211−17 (3C 444) is a LERG with cavities around its FRII lobes and a large-scale shock at about 200 kpc (Croston et al. 2011). It lies in a rich environment ($B_{gq} \sim 1300$ — Ramos Almeida et al. 2013). We obtained a similar temperature profile to that of Croston et al. (2011). For this work, we used a temperature within an annulus excluding the central temperature dip and extending across a wider region, and our temperature and luminosity are consequently a little higher ($4.11^{+0.18}_{-0.18}$ vs 3.5 ± 0.2 keV and $2.86^{+0.02}_{-0.03}$ vs 1.0×10^{44} erg s^{-1}).

PKS 2221−02 (3C 445) is a BLRG with FRII morphology which is thought to have disc winds coming from the central regions (Braito et al. 2011). Ramos Almeida et al. (2013) found a weak environment ($B_{gq} \sim 50$). We had insufficient counts left after subtraction of the *Chandra* blank sky files to obtain a background for the spectral analysis, so we used single background subtraction for the temperature. Our temperature is that of a group (1.1 keV), and is consistent with that found by Hodges-Kluck et al. (2010).

PKS 2356−61 is an NLRG with FRII lobes in a group environment ($B_{gq} \sim 450$ – Ramos Almeida et al. 2013). There were insufficient counts left after subtraction of the *Chandra* blank sky files to obtain a background for the spectral analysis. We therefore used single subtraction using a background from the observing chip to obtain the temperature, which was that of a group (1.2 keV). Hodges-Kluck et al. (2010) found a two-temperature ICM (3.0 and 0.9 keV) but used a much smaller radius for the spectrum. We could not fit a second thermal component with our wider region.